On the optimal morphology and performance of a modeled dragonfly airfoil in gliding mode

Cite as: Phys. Fluids **31**, 051904 (2019); https://doi.org/10.1063/1.5093230
Submitted: 19 February 2019 . Accepted: 22 April 2019 . Published Online: 14 May 2019

Mohd Imran Ansari, Mohammed Hamid Siddique, Abdus Samad, and Syed Fahad Anwer

Physics of Fluids ARTICLE scitation.org/journal/phf

On the optimal morphology and performance of a modeled dragonfly airfoil in gliding mode

Cite as: Phys. Fluids 31, 051904 (2019); doi: 10.1063/1.5093230
Submitted: 19 February 2019 • Accepted: 22 April 2019 •
Published Online: 14 May 2019

Mohd Imran Ansari,[1] Mohammed Hamid Siddique,[2] Abdus Samad,[3] and Syed Fahad Anwer[1,a)]

AFFILIATIONS

[1]Computational Aerodynamics Lab, Department of Mechanical Engineering, ZHCET, Aligarh Muslim University, Aligarh 202002, India
[2]Department of Mechanical Engineering, ADCET, Ashta, Maharashtra 416301, India
[3]Department of Ocean Engineering, IIT Madras, Adyar, Chennai, Tamil Nadu 600036, India

[a)]**Author to whom correspondence should be addressed:** sfahadanwer@zhcet.ac.in. **Tel.:** +91-8126634354.

ABSTRACT

Numerical investigation on the effect of wing morphology of the dragonfly *Aeshna cyanea* is carried out to understand its influence on the aerodynamic performance. The two-dimensional wing section has corrugation all over the surface along the chord length on both upper (suction side) and lower (pressure side) surfaces. By considering each corrugation separately on different airfoils at their different positions, 10 single corrugated airfoils were generated. Simulations are performed on these different airfoils to determine the effect of each corrugation on aerodynamic performance. The flow is modeled as incompressible, Newtonian, homogeneous, and unsteady. The angle of attack was varied from 0° to 20°, and the Reynolds number (Re) was varied from 150 to 10 000. The optimum morphology and angle of attack were predicted by using the surrogate-based optimization technique for a maximum gliding ratio at different Re. A fully corrugated pressure side gives the best performance at angles of attack of 9.79° and 14.83° at low Re. At high Re, corrugations on the pressure side which are in the middle and those near the trailing edge give a maximum gliding ratio at angles of attack 9.22° and 5.276°. The spatiotemporal dynamics indicate that corrugations near the leading edge on the upper surface and corrugations near the trailing edge for the lower surface and which are in the middle are beneficial. It is also found that shear drag due to corrugation decreases but pressure drag increases; therefore, the overall drag coefficient for a fully corrugated airfoil increases. Corrugations on the suction side have little influence, while those on the pressure side causes lift enhancement.

NOMENCLATURE

c	=	chord length of the airfoil
$\bar{C}_D$	=	time averaged mean drag coefficient
$\bar{C}_{SF}$	=	time averaged mean skin friction coefficient
$\bar{C}_{DP}$	=	time averaged mean pressure drag coefficient friction coefficient
$\bar{C}_L$	=	time averaged mean lift coefficient
$\bar{C}_L/\bar{C}_D$	=	gliding ratio
C_p	=	$(p - p_i)/(p_o - p_i)$
F_D	=	drag force
F_L	=	lift force
l_{rel}	=	relative span length
p	=	pressure
Re	=	chord based Reynolds number
u	=	x-component velocity
U_∞	=	free stream velocity

I. INTRODUCTION

In recent years, research on insect flight became a topic of great importance to understand its mechanism for the development of Micro-Air-Vehicles (MAVs) due to their wide range of applications. MAVs are portable small-sized vehicles used for surveillance at low altitude and have acquired significant attraction in civil and military applications. These vehicles are equipped with video cameras and transmitters to transmit images of the places where humans cannot reach. MAVs with an array of sensors are also capable of obtaining additional information such as chemical and radiation levels in the environment. The size of MAVs is as small as 15 cm, weight about

90 g, and have a flight speed of about 10 m/s. The idea behind the design of MAVs is borrowed from the flight of insects. A number of insect wings have well-defined corrugated configurations. These well-defined corrugated structures of the wing are of great significance in terms of high stiffness against spanwise bending while allowing torsion and formation of camber to occur (Rees, 1975 and Newman *et al.*, 1977).

Gliding flight mode is the widely used power saving technique for MAVs as it requires no energy consumption (Vargas and Mittal, 2004). Gliding flight is also frequently observed in dragonflies. A dragonfly has the capability of both hovering and gliding motion. Using flapping motion, the dragonfly elevates into the air, and by consuming the potential energy, it glides horizontally above the ground (Brodsky, 1994). Due to the high aspect ratio of the wing, it has a superior gliding flight and spends less energy in comparison to other insects (Ennos, 1989). With the increase in ambient temperature, the time spent by the dragonfly for gliding flight increases and the flapping frequency declines considerably (Hankin, 1921; May, 1978; and 1995). The flapping frequency usually lies between 30 and 50 Hz (Ruppell, 1989), and the motion of the forewing and hindwing is independent (Alexander, 1984). Some smaller dragonflies have gliding flight time of about 0.5 s with a travel distance of about 1 m in this interval and have a maximum speed of about 2.6 m/s (Wakeling and Ellington, 1997). The gliding time interval of the dragonfly genus *Aeshna* is about 30 s without any appreciable loss in altitude (Brodsky, 1994). The flight of the dragonfly is observed at an ultralow Reynolds number (Re) flow regime that ranges from 100 to 10 000 (Wakeling and Ellington, 1997).

Rees (1975) and Rudolph (1977) conducted wind tunnel experiments on the corrugated wings. They found that the flow flowing over the wing is trapped in the valleys of corrugation and where this trapped fluid remains stagnant or rotated slowly. They concluded that no advantage of corrugation on the aerodynamic performance is observed. Rudolph (1977) found only the advantage of the corrugated wing over a smooth airfoil at a high angle of attack as the delay in the separation of flow occurs for the corrugated airfoil. Furthermore, Murphy and Hu (2010) conducted an experimental study on a bioinspired corrugated airfoil having sharp edges by considering the dragonfly (*Aeshna cyanea*) profile. For experimental testing in the wind tunnel, the corrugated profile was fabricated out of the wooden plate. The aerodynamic forces were calculated for Re = 58 000–125 000 and compared with a streamlined and flat plate airfoil. They reported that the corrugated airfoil generates higher lift as compared to the streamlined airfoil and flat plate, and a delay in flow separation occurs for a high angle of attack. With the help of a particle image velocimetry system, it was found that the transition of flow from laminar to turbulent occurs due to the peak of corrugation, and the unsteady vortex is trapped in the valleys. Due to these trapped vortices, the turbulent flow remained attached to the surface of the wing. The detailed aerodynamic study to compare a bioinspired corrugated airfoil, a low-speed NASA GA (W)-1 airfoil, and a flat plate at Re = 3.4×10^4 was carried out by Hu and Tamai (2008). They found that the corrugated profile having protruding corners acts as turbulators due to which the separated shear-layer flow transits from laminar to turbulent. The vortices formed by the turbulent shear layer carried kinetic energy from outside to near wall regions and reduced the large-scale flow separation, which enhances the lift due to corrugations. Kesel (2000) experimentally analyzed the forewing of the dragonfly (*Aeshna cyanea*) at three locations (30%, 50%, and 70%) of the span at Re = 10 000 and compared it with a smooth profile (constructed by drawing a smooth envelope through the corners of the corrugated airfoil) and a flat plate. It was reported that the corrugated profile produces negative pressure in the valleys of upper and lower surfaces and, thus, have a much higher lift coefficient. But the effect of different pleats and their position on the performance of the airfoil was not investigated. Numerical investigations of the dragonfly's wing section were also carried out by Vargas *et al.* (2008). The sharp interface Cartesian-grid-based immersed boundary technique was used at ultralow Reynolds numbers. It was found that the negative shear drag is produced within the pleats of the corrugated wing section by the recirculation zone which is accounted for the reduction of overall drag. In this pleated airfoil, higher lift and moderate drag lead to an aerodynamic performance at least equivalent or better than the profiled airfoil. Finally, it was concluded that the pleated wing is an ingenious design of nature which at times surpasses the aerodynamic performance of a more conventional airfoil and flat plate. Lee and Kim (2017) experimentally investigated the flow structure of translating a comblike wing having a wide range of gap sizes. They found that the comblike plate generated larger aerodynamic force per unit area as compared to the smooth plate. Bose and Sarkar (2018) studied flow transition from periodic to chaotic through the quasiperiodic route. It was reported that, as the plunge amplitude was gradually increased (NACA0012), in the low Reynolds number regime, the flow transitions itself from periodic to quasiperiodic. Leading edge separation plays a key role in providing the first trigger in aperiodicity. Lee *et al.* (2018) numerically investigated a two-dimensional bristled wing model and found that the aerodynamic force generated by each bristle behaves independently and produces similar force due to strong gap flows relative to the wing at a high Reynolds number, while each bristle experiences different forces depending on the relative position at a low Reynolds number. Newman *et al.* (1977) reported the enhancement in aerodynamic performance due to earlier reattachment of flow on the surface of the corrugated wing. As the angle of attack increases, separation of the flow takes place from the leading edge and is reattached near the trailing edge earlier in the case of the corrugated wing as compared to smooth airfoils, forming the separation bubble in the region of separation. In the flapping flight or hovering regime, Xu *et al.* (2017) analyzed the propulsive performance of two flapping foils in tandem configurations. They observed that the propulsive performance of tandem foils affects significantly at various longitudinal distances and phase differences. Peng *et al.* (2018) numerically investigated the collective locomotion of a pair of plates of comparable but different propulsive capabilities and found that two equilibrium configurations, compact and sparse, may emerge, depending on initial lateral H and longitudinal gap G_o spacing. The propulsive performance of the leading-edge plate is the same as the isolated one in all sparse configuration. Shahzad *et al.* (2018) performed simulations to find the effect of hawkmothlike flexibility on aerodynamic hovering performance at Re = 400. They also estimated the optimum combination of the shape, AR, and flexibility to maximize the power and economy. Han *et al.* (2019) investigated the interaction of wake produced by two flapping wings and found that interaction reduces the aerodynamic force, regardless of the shape of the motion profile at zero reduced angles. From the literature discussed earlier, most authors found that lift increases due to corrugation and some

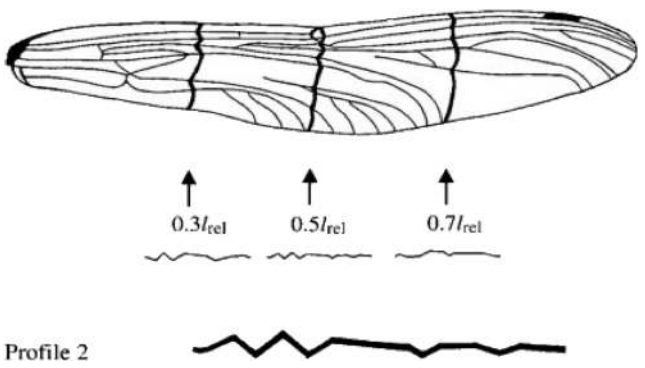

FIG. 1. Forewing of the dragonfly (*Aeshna cyanea*) and profile 2 at 0.5l_{rel} section of the wing (Kesel, 2000).

authors also found no advantage of corrugation. But none of the authors discussed the effect of separate corrugation or their location on the surface of the airfoil on its aerodynamic performance.

In this paper, we try to investigate the optimum morphology for a maximum lift to drag ratio in gliding flight. For this purpose, a 2d wing section at 50% relative span length from the wing base of the dragonfly *Aeshna cyanea* is extracted as given in Kesel (2000) (Fig. 1). The wings of *Aeshna cyanea* have corrugation on both upper and lower surfaces. By drawing smooth curves from extreme edges, a smooth airfoil is constructed. Then, by taking every single corrugation at their respective position on the smooth airfoil, 10 airfoils having single corrugation on the surface are created as shown in Fig. 2. A numerical study is carried out to find the influence of each corrugation. These profiles are further discussed in Sec. II. Further by taking the upper surface corrugated and lower smooth and vice versa, the effects of corrugation on the suction and pressure sides are also evaluated. Direct numerical simulation is carried out for the aerodynamic performance of various airfoils for forward flight in the gliding mode. The problem is also to optimize a single objective function, i.e., to maximize $\bar{C}_L/\bar{C}_D$ at different Reynold numbers 150, 1400, 6000, and 10 000. The design parameters at each Reynolds number are the shape of airfoils (SM, CR, M1-M6, and N1-N6) and the angle of attack (α). Among different shapes of the airfoil, it is difficult to find out which shape and angle of attack combination at a particular Reynolds number gives the best aerodynamic performance. To the best of the authors' knowledge, this is the first investigation on the determination of optimum morphology at different Reynolds numbers.

II. MATHEMATICAL METHODS

A. Governing equations

The time-dependent Navier Stokes equation, governing the viscous incompressible flow, is solved using the Ansys Fluent solver. The continuity and momentum equations are as follows:

$$\text{Continuity}: \nabla \cdot \vec{\mathbf{u}} = 0, \tag{1}$$

$$\text{Momentum}: \frac{\partial \vec{u}}{\partial t} + (\vec{u} \cdot \nabla)\vec{u} = -\frac{1}{\rho}\nabla p + \nu \nabla^2 \vec{u}. \tag{2}$$

The nondimensional parameter "Reynolds number (Re)" is based on chord length c, free stream velocity U∞, and kinematic viscosity ν, which is defined as

$$Re = \frac{U_\infty c}{\nu}. \tag{3}$$

B. Numerical method

The governing equation for the flow is solved by the finite volume method (FVM). The staggered cell-centered approach is used along with projection methods as the pressure-velocity coupling scheme with an implicit time stepping scheme.

The projection method (Chorin, 1968; Armfield and Street, 1999; Dukowwicz and Dvinsky, 1992; Glaz *et al.*, 1989; and

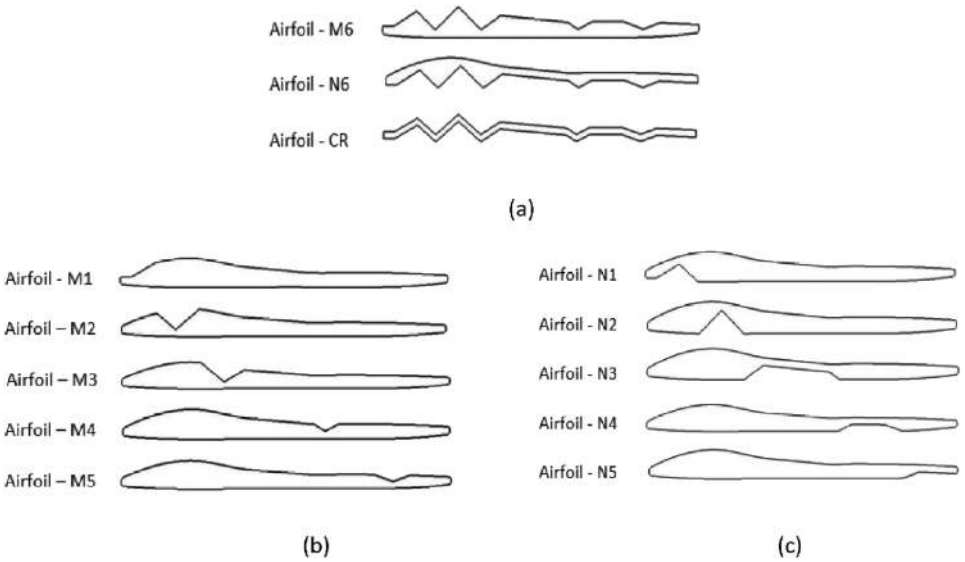

FIG. 2. Airfoil geometries (a) smooth airfoil-SM, upper surface corrugated airfoil-M6, lower surface corrugated airfoil-N6, and corrugated airfoil-CR. (b) Airfoils having single corrugation on the suction side. (c) Airfoils having single corrugation on the pressure side.

Perot, 1993) is used to solve the above continuity and momentum equations in which the equations are advanced in time by a fractional step as given below.

Ignoring the pressure gradient term, first compute the intermediate velocity u^*,

$$\frac{u^* - u^n}{\Delta t} = -\left(u^n \cdot \nabla\right)u^n + \nu\nabla^2 u^n. \tag{4}$$

In order to obtain the final solution of the time step u^{n+1}, intermediate velocity u^* is corrected as

$$u^{n+1} = u^* - \frac{\Delta t}{\rho}\nabla p^{n+1}. \tag{5}$$

Rewrite Eq. (5) in the form of time step as

$$\frac{u^{n+1} - u^*}{\Delta t} = -\frac{1}{\rho}\nabla p^{n+1},$$

where superscripts n and n + 1 denote the solution at current and next time step, respectively.

In Eq. (5), the knowledge of pressure "p" at (n + 1) time level is required. Therefore, by taking divergence (continuity condition) at (n + 1) time level, $\nabla \cdot u^{n+1} = 0$ and applying projector equation to Eq. (5).

The following Poisson equation is derived for p^{n+1}:

$$\nabla^2 p^{n+1} = \frac{\rho}{\Delta t}\nabla \cdot u^*. \tag{6}$$

After solving the Poisson equation using the Gauss-Seidel-type algebraic multigrid method for pressure at n+1 time step, the velocity field can be updated by Eq. (5).

The convective and diffusive terms are discretized using the Quadratic Upstream Interpolation for Convective Kinetics (QUICK) scheme, which is the second order central difference for the diffusive term and third order accurate in space and first order in time for the convective term. The boundary condition having fluid velocity at the inlet, pressure at the outlet, and wall on the airfoil surface with no slip boundary is applied.

C. Airfoil geometries

The forewing of the dragonfly (*Aeshna cyanea*) used in Kesel (2000) experiment is shown in Fig. 1. The airfoil having cross section at the mid of the span (l_{rel} = 0.5 from the wing base), here named airfoil-CR, is considered for the morphological study of the wing. This particular cross section in Kesel's experiment is considered as profile 2. The leading edge of this typical profile is straight. First, a smooth airfoil (named as SM) is constructed by drawing a smooth envelope of line through the sharp edges of the corrugated airfoil CR. Further 10 other airfoils are constructed, on the suction side (named M1, M2, M3, M4, and M5) and on the pressure side (named N1, N2, N3, N4, and N5) by placing each corrugation separately at their respective position on the surface of the smooth airfoil SM. In addition, an airfoil (M6) having the suction side fully corrugated and the pressure side smooth, and similarly airfoil (N6) having the pressure side fully corrugated and the suction side smooth is added in the study. The position of corrugation on the suction side from the leading edge is 0.035c (M1), 0.167c (M2), 0.312c (M3), 0.618c (M4), and 0.823c (M5). For the pressure side, the positions are 0.109c (N1), 0.240c (N2), 0.373c to 0.585c (N3), 0.661c to 0.764c (N4) and 0.876c (N5) from the leading edge. Naming of the airfoil is done as shown in Fig. 2. All the airfoils have thickness to chord length ratio t/c = 7.531%.

D. Optimization

1. Surrogate models

A surrogate model is an approximation model that mimics the behavior of high fidelity numerical models such as experimental or Computational Fluid Dynamics (CFD) results to fit the curve as closely as possible. The surrogate models such as radial basic neural network (RBNN), Kriging (KRG), and response surface approximation (RSA) are some of the commonly used in the area of aerospace, medical science, and engineering designs.

(a) Radial basic neural networks (RBNNs): The RBNN is a double layered network consisting of an intermediate hidden layer of radial basis functions acting similar to neurons. The radial basis functions act as processing units between the input and output. The main advantage of using the radial basis approach is the ability to reduce the computational cost owing to the linear nature of radial basis functions.

(b) Kriging (KRG): Kriging model is a geostatistics based approximation function which works on the weighted superposition of the Gaussian function which can be expressed as an unknown function F(x) can be given by

$$F(x) = y(x) + m(x), \tag{7}$$

where y(x) is the known global function and m(x) represents a local deviation from the global model.

(c) Response surface approximation (RSA): The response surface approximation method (RSA) is a statistical method to explore the relationship between variables and objectives.

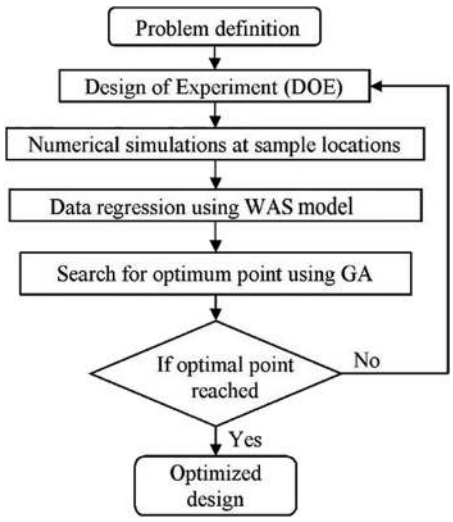

FIG. 3. Single objective optimization flow chart.

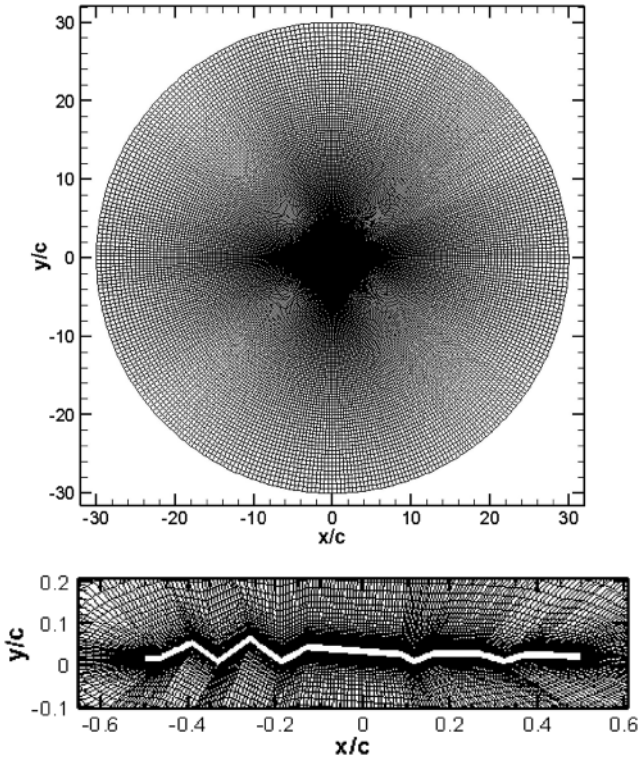

FIG. 4. Nonuniform structured o-grid around the corrugated airfoil in the circular domain and close view grid near the airfoil.

This model can be expressed by a polynomial function as

$$y = F(x) = y(x_1, x_2) + e, \tag{8}$$

where y is the objective function of variables x_1 and x_2 with an approximation error "e."

Any poorly fitted surrogate may lead to unreliable results. Averaging of surrogate model works can generate a new type of approximation model called weighted-average surrogate (WAS) model which can reduce the effect caused due to bad surrogate predictions. The WAS model can be represented as (Goel *et al.*, 2007)

$$F_{WAS}(x) = \sum_i^m w_i(x) F_i(x), \tag{9}$$

where $F_{WAS}(x)$ is the predicted response of the WAS model at the x design location. $F_i(x)$ is the predicted response of a surrogate model used in averaging, and $w_i(x)$ is the weightage of the mth surrogate model at the design point x. The sum of all the weights should be equal to 1.

In this study, the surrogate models used are the response surface approximation (RSA), Kriging (KRG), and radial basis neural network (RBNN). So, the WAS model is based on these surrogates, which can be written as

$$F_{WAS}(x) = w_{RSA} F_{RSA}(x) + w_{KRG} F_{KRG}(x) + w_{RBNN} F_{RBNN}(x), \tag{10}$$

where, w_{RSA}, w_{KRG}, and w_{RBNN} are the weights associated with the surrogates RSA, KRG, and RBNN, respectively. $F_{RSA}(x)$, $F_{KRG}(x)$, and $F_{RBNN}(x)$ are the predicted response of the surrogate for (x) design points.

There are many methods to find weights (w) for a surrogate, and the most common methods by Goel *et al.* (2007) are based on global data-based selection on the magnitude of errors. The weightage scheme used in this work can be expressed as

$$w_i = \frac{\sum_{j=1, j\neq i}^{m} e_j}{(N-1)\sum_{j=1}^{m} e_j}, \tag{11}$$

where e_j is the global database error measure of the jth surrogate model. The best fitted surrogate of mth models will give least error, i.e., close to zero give weight to that surrogate close to 1.

2. Single objective optimization

A single-objective optimization (SOO) is considered if one of the objective functions dominates the others. In this case, the other objective can be taken as constraints. The optimized procedure followed has been shown with the help of a flow chart in Fig. 3.

3. Data regression using WAS model

The results generated by the sample designs were tabulated and were used to train the surrogates RSA, KRG, and RBNN, respectively. Each surrogate models generate their own feasible design point with some fitting errors. Based on these errors, a weighted average surrogate (WAS) was constructed to generate a feasible design point, and with the help of genetic algorithm GA, the optimum point was obtained. This optimum point was validated using CFD results to check its convergence. If the WAS optimum point converges with CFD, then we get the final design or else step 2 is repeated.

4. Genetic algorithm based search technique

To find the optimum design, an evolutionary algorithm (EA) such as genetic algorithm (GA) is used. The GA mimics natural

TABLE I. Grid independence test for airfoil-CR at angle of attack α = 4° with Re = 6000.

Airfoil-CR, Re = 6000 and angle of attack α = 4°						
S. no.	Quadrilateral cells	Grid size	$\bar{C}_L$	$\bar{C}_D$	% change in $\bar{C}_L$	% change in $\bar{C}_D$
1	50 622	0.0005	0.3475	0.0693	...	...
2	70 446	0.0001	0.3583	0.0709	3.097	2.483
3	105 492	0.000 05	0.3641	0.0727	1.619	2.474

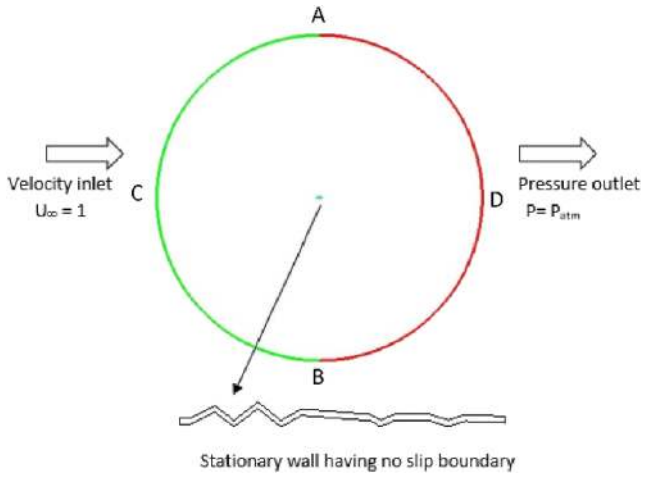

FIG. 5. Computational domain with boundary conditions.

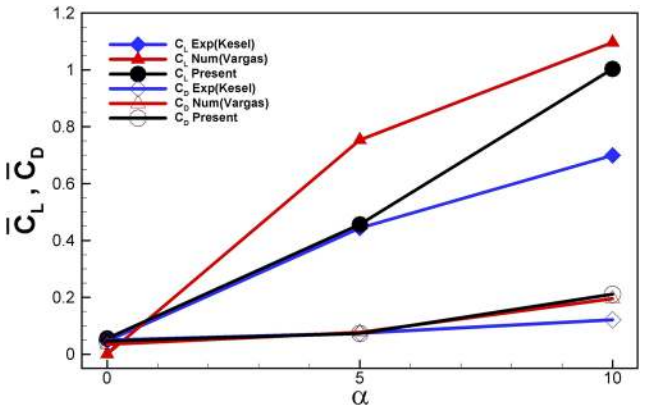

FIG. 6. Comparison of $\bar{C}_L$ and $\bar{C}_D$ at various angles of attack and Re = 10 000 for the corrugated airfoil.

evolutionary concepts to constitute a search and optimization procedure (Deb, 2004). The GA is based on the mechanics of natural selection and mutation and is a blind search method which uses only information related to the objective function (McCall, 2005). The main components of GA are chromosome encoding, fitness function, selection, recombination, and the evolution scheme. This GA is coupled with WAS to obtain an optimum design point within the feasible solution.

III. COMPUTATIONAL DOMAIN AND BOUNDARY CONDITIONS

The computational domain, the region where the discretized differential equations are solved, is an important parameter for the numerical simulation of fluid flow problems. The boundary of the domain grid should be sufficiently far away from the airfoil such that its effect is minimum on the numerical simulation. In the present case, the domain is circular with the airfoil at its center. The diameter of the domain is 60c, which is finally selected after comparing with the domain of diameter 40c, 60c, and 80c having the value of the force coefficient less than 0.5% between 60c and 80c. The O-type structured nonuniform grid is formed around the airfoil, and a close view near the airfoil is shown in Fig. 4. For the study of grid independence, three grids of size 50 622, 70 446, and 105 492 quadrilateral cell are considered. The results obtained at these grids at 4° angle of attack and Re = 6000 are tabulated in Table I. The computational grid of size 70 446 (354*199) quadrilateral cell is finally selected as the changes in the force coefficient are less than 5% between the last two grids.

To have accurate results, grid resolutions are important. The minimum grid size near the surface wall is Δs = 0.0001 for all Reynolds numbers. For Re = 10 000 (at the largest Re considered, where the boundary layer is thinnest), the calculated value of minimum s+ is 0.059 (near wall spacing in terms of classical scaling) and there are 10 grid points in between the surface of the airfoil and s+ = 1.0. For Re = 150 (at the smallest Re considered, where the boundary layer is thick), the value of minimum s+ is 0.0012 and there are 32 grid points in between the surface of the airfoil and s+ = 1.0. Therefore, the grid resolution for numerical simulation is suitable for accurate results. For external flows, when the Reynolds number is above 10 000, the turbulent regime should be considered in the numerical simulation, but most of the insect flight is in the laminar flow regime, and here, the main objective of our study is to investigate the influence of corrugation on the surface of the airfoil, so we assume laminar flow for the numerical simulation. A similar type of assumptions was also adopted by Kim *et al.* (2009). All simulation is run at a 70 446 quadrilateral cell grid and at a uniform time step of 0.0005c/U∞.

TABLE II. Numerical values of $\bar{C}_L$ and $\bar{C}_D$ for NACA0004 in comparison with those of Kunz and Kroo (2001) for Re = 2000 and 6000 at α = 0° and 4°.

Angle of attack (deg)	α = 0°				α = 4°			
Reynolds number	Re = 2000		Re = 6000		Re = 2000		Re = 6000	
	$\bar{C}_L$	$\bar{C}_D$	$\bar{C}_L$	$\bar{C}_D$	$\bar{C}_L$	$\bar{C}_D$	$\bar{C}_L$	$\bar{C}_D$
Numerical results	. . .	0.071 02	. . .	0.039 68	0.3191	0.076	0.3315	0.044 03
Kunz and Kroo (2001)	. . .	0.0704	. . .	0.0392	0.335	0.0749	0.3439	0.0427
Percentage difference (%)	. . .	0.88	. . .	1.22	4.74	1.18	3.6	3.11

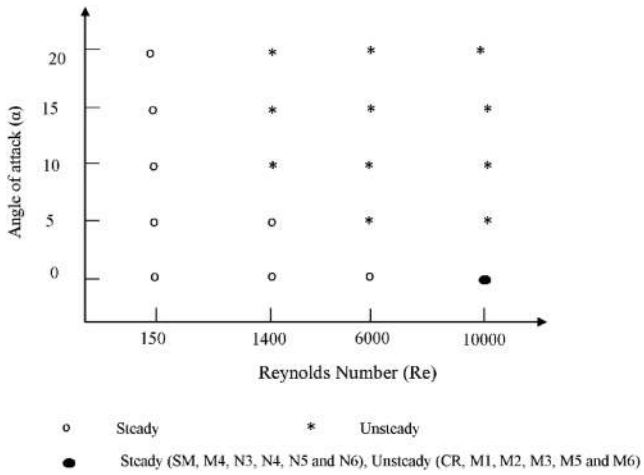

FIG. 7. Regime map for steady and unsteady nature for various angles of attack and Reynolds numbers.

The 2D domain has two boundary conditions located at left ACB and right ADB of the computational domain. A Dirichlet boundary condition is defined as the inlet fluid velocity of the domain at the left half-circle ACB, while the right half-circle ADB as pressure outlet $p = p_\infty$ and velocity is interpolated, applied as the boundary condition as shown in Fig. 5. On the airfoil surface, no-slip boundary is applied. The normal momentum equation is used to update pressure.

IV. VALIDATION

In order to validate the current pressure based solver, the numerical simulation for the flow past the NACA0004 airfoil is performed and the results are compared with those of Kunz and Kroo (2001). The results of interest are the lift and drag coefficients. The time-averaged lift and drag coefficients at 0° and 4° angles of attack and Re = 2000 and 6000 are tabulated in Table II. Table II shows that the deviation in $\bar{C}_L$ and $\bar{C}_D$ for the NACA 0004 airfoil by our solver and Kunz and Kroo (2001) has the difference less than 5% for all four cases. This means that the current methodology is validated. Furthermore, the results are also compared for the corrugated airfoil with the experimental results of Kesel (2000) and the numerical results with those of Vargas *et al.* (2008). Figure 6 shows that the present $\bar{C}_L$ and $\bar{C}_D$ are in good agreement up to angle of attack 5°.

V. RESULTS AND DISCUSSION

The unsteady flow analysis is carried out for different 2D airfoils to study the effect of morphology by considering corrugation on the suction and pressure sides in comparison with the smooth airfoil. The Reynolds numbers used in this study are 150, 1400, 6000, and 10 000. The angle of attack α ranges between 0° and 20°. Newman *et al.* (1977), Okamoto *et al.* (1996), and Kesel (2000) compared the experimental studies carried out on the dragonfly wing and airfoils at Re = 10 000. In Subsections V A–V F, the nature of flow around airfoils, the effect of corrugation on shear and pressure drag, the effect of each separate corrugation on lift and drag, and the optimized value of the shape of the airfoil and the angle of attack for higher

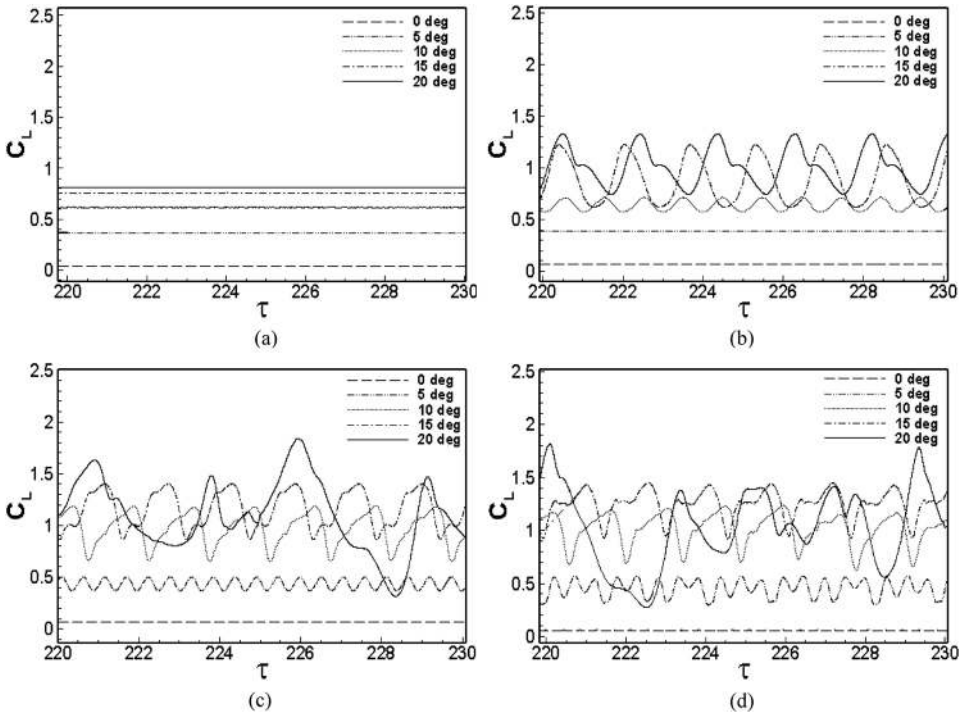

FIG. 8. Time histories of the lift coefficient for airfoil-CR at (a) Re = 150, (b) Re = 1400, (c) Re = 6000, and (d) Re = 10 000.

values of $\bar{C}_L/\bar{C}_D$ at different Reynolds numbers are discussed and evaluated.

A. Lift and drag coefficient

The derived quantities in the study are lift and drag coefficients, which is the measure of the aerodynamic performance of the wing and defined as

$$\text{Lift coefficient} \quad C_L(t) = \frac{F_L(t)}{1/2\rho U_\infty^2 c}, \tag{12}$$

$$\text{Drag coefficient} \quad C_D(t) = \frac{F_D(t)}{1/2\rho U_\infty^2 c}. \tag{13}$$

The corresponding mean value of lift and drag coefficients is calculated by taking the time average of the transient stationary part of $C_L(t)$ and $C_D(t)$,

$$\text{Mean lift coefficient} \quad \bar{C}_L = \frac{1}{T - t_o}\int_{t_o}^{T} \frac{F_L(t)}{1/2\rho U_\infty^2 c}\mathrm{dt}, \tag{14}$$

$$\text{Mean drag coefficient} \quad \bar{C}_D = \frac{1}{T - t_o}\int_{t_o}^{T} \frac{F_D(t)}{1/2\rho U_\infty^2 c}\mathrm{dt}, \tag{15}$$

where t_o is the time at which the transient stationary state for simulation is started and $(T - t_o)$ is the time for 20 cycles of oscillations.

The morphological study of a 2D section wing of the dragonfly (*Aeshna cyanea*) is carried out by analyzing the aerodynamic performance in the low Reynolds number regime. If the time history of lift or drag is a straight line or oscillatory, then the nature of the flow is steady or unsteady, respectively. The nature of the flow (steady or unsteady) remains the same for airfoils at similar various angles of attack and Reynolds numbers. However, at Re = 10 000 and angle of attack $\alpha = 0°$, the effect of different corrugations on the nature of flow comes into play and have different nature for different airfoils. A flow regime map at various angles of attack and Reynolds numbers is shown in Fig. 7.

The time histories of the lift coefficient with time for airfoil-CR at different Reynolds numbers and angles of attack are shown

TABLE III. Time averaged mean force coefficient and gliding ratio at angle of attack $\alpha = 0°$ and Re = 150, 1400, 6000, and 10 000.

Airfoil	$\bar{C}_L$	$\bar{C}_{DS}$	$\bar{C}_{DP}$	$\bar{C}_D$	$\bar{C}_L$	$\bar{C}_{DS}$	$\bar{C}_{DP}$	$\bar{C}_D$
Angle of attack $\alpha = 0°$ and Re = 150					Angle of attack $\alpha = 0°$ and Re = 1400			
SM	0.0336	0.2619	0.0527	0.3147	0.0515	0.0692	0.0243	0.0935
M1	0.029	0.2575	0.0566	0.3141	0.0488	0.0664	0.0271	0.0935
M2	0.0274	0.2483	0.0648	0.3130	0.0440	0.0625	0.0314	0.0939
M3	0.0307	0.2556	0.0581	0.3137	0.0481	0.0668	0.0272	0.0940
M4	0.0331	0.2604	0.0542	0.3147	0.0507	0.0690	0.0247	0.0936
M5	0.0486	0.2601	0.0537	0.3137	0.0589	0.0686	0.0246	0.0932
M6	0.0136	0.2205	0.0926	0.3131	0.0363	0.0498	0.0460	0.0959
N1	0.0403	0.2471	0.0663	0.3133	0.0552	0.0626	0.0309	0.0935
N2	0.0370	0.2540	0.0597	0.3137	0.0548	0.0659	0.0278	0.0938
N3	0.0432	0.1910	0.1229	0.3139	0.0659	0.0649	0.0291	0.0940
N4	0.0350	0.2582	0.0556	0.3138	0.0582	0.0675	0.0259	0.0933
N5	0.0284	0.2596	0.0540	0.3136	0.0412	0.0681	0.0249	0.0930
N6	0.0604	0.2115	0.0998	0.3113	0.0766	0.0457	0.0482	0.0940
CR	0.0405	0.1699	0.1405	0.3104	0.0619	0.0263	0.0702	0.0965
Angle of attack $\alpha = 0°$ and Re = 6000					Angle of attack $\alpha = 0°$ and Re = 10 000			
SM	0.0712	0.0275	0.0168	0.0442	0.0981	0.0189	0.0153	0.0342
M1	0.0756	0.0246	0.0197	0.0444	0.1023	0.0162	0.0186	0.0348
M2	0.0555	0.0237	0.0228	0.0465	0.0637	0.0163	0.0217	0.0381
M3	0.0518	0.0278	0.0181	0.0459	0.0450	0.0211	0.0157	0.0368
M4	0.0722	0.0276	0.0168	0.0444	0.0991	0.0192	0.0151	0.0343
M5	0.0719	0.0271	0.0170	0.0441	0.1041	0.0187	0.0156	0.0343
M6	0.0514	0.0158	0.0342	0.0500	0.0484	0.0105	0.0328	0.0432
N1	0.0740	0.0235	0.0214	0.0448	0.1028	0.0156	0.0198	0.0354
N2	0.0769	0.0256	0.0197	0.0453	0.1059	0.0175	0.0182	0.0357
N3	0.0843	0.0242	0.0210	0.0451	0.1097	0.0161	0.0192	0.0353
N4	0.0819	0.0260	0.0184	0.0443	0.1066	0.0175	0.0171	0.0346
N5	0.0587	0.0265	0.0174	0.0439	0.0832	0.0180	0.0160	0.0340
N6	0.0888	0.0125	0.0341	0.0466	0.1128	0.0068	0.0307	0.0375
CR	0.0661	0.0012	0.0511	0.0524	0.0557	−0.0011	0.0474	0.0463

in Fig. 8. At Re = 150, the flow is steady and C_L increases with a rise in the angle of attack, but the amount of rising in C_L drops. At Re = 1400, the nature of flow is steady up to 5° angle of attack. At 10° and as the angle of attack increases, the flow becomes unsteady in nature. The amplitude of oscillation increases and frequency decreases with an increase in the angle of attack. The nature of flow becomes oscillatory at α = 5° for Re = 6000, and the flow is oscillatory even at α = 0° at Re = 10 000 for airfoil-CR. The transition from steady to unsteady occurs at a lower angle of attack as the Reynolds number increases.

B. Effect of angle of attack

First, the aerodynamic performance is investigated at the angle of attack α = 0° for different airfoils. The time-averaged mean force coefficient corresponding to different airfoil geometries is tabulated in Table III. The total mean drag coefficient decreases with an increase in the Reynolds number. The reason for the decrease in the total mean drag is due to an appreciable decline in shear drag while the drop in the pressure drag is small in comparison to the shear drag. It clearly indicates that viscous forces which are

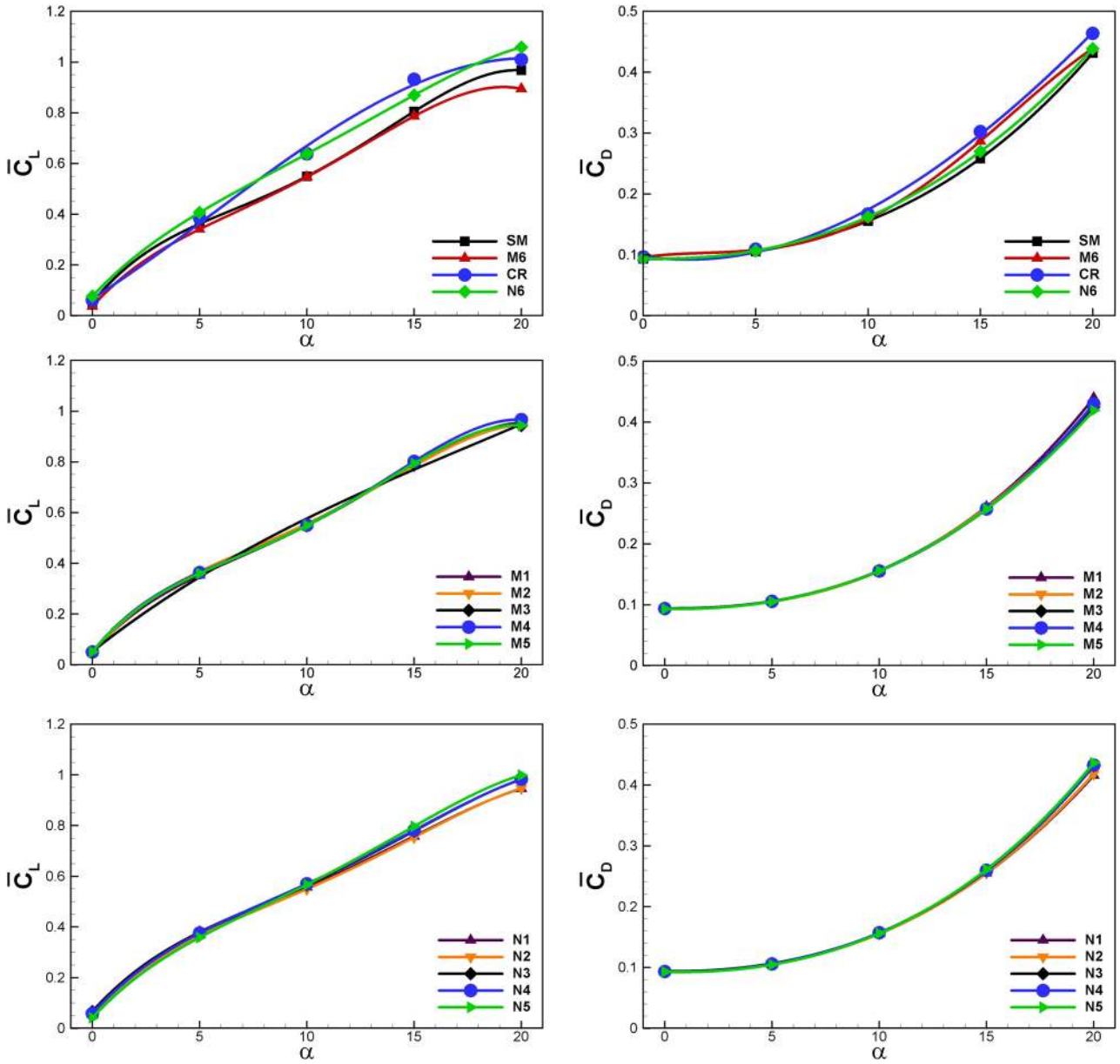

FIG. 9. Variation of the time averaged mean lift and drag coefficients with the angle of attack for various airfoils at Re = 1400.

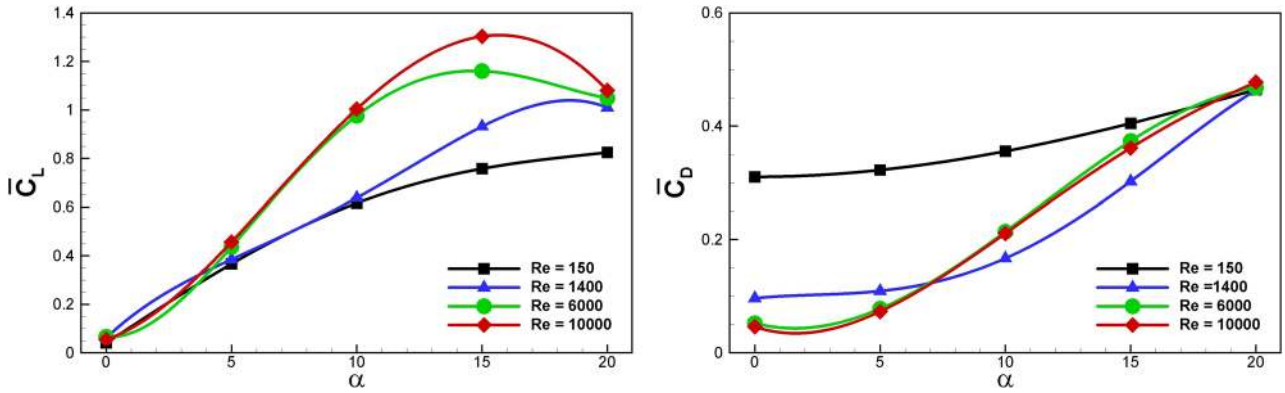

FIG. 10. Variation of the time averaged mean lift and drag coefficient with the angle of attack for airfoil-CR at various Reynolds numbers.

dominant at a low Reynolds number become weak with the increase in the Reynolds number. The pressure drag due to the wake region is created by the fluid behind the airfoil and is less sensitive to the Reynolds number.

Comparing the shear drag for different airfoils, the highest percentage of shear drag is 83% of total drag and found for a smooth airfoil SM at Re = 150 and the lowest percentage is 2.3% and found for airfoil CR at Re = 6000. At high Reynolds number Re = 10 000, a negative shear drag is found for airfoil CR, signifying the thrust generation. The airfoil CR has the lowest percentage of shear drag among all airfoils at various Reynolds numbers, but it has the highest total drag due to a rise in the pressure drag at Re = 1400 and higher. The largest shear drag at Re = 150 and 1400 is found for airfoil SM. At Re = 6000 and 10 000, a largest shear drag was found in airfoils having corrugation at the mid and trailing edge airfoils (M3, M4, and M5) having the similar highest value. Among the airfoils having single corrugation on the suction side, the airfoil M2 has the lowest shear drag. The shear drag of N1 and M2 is also nearly the same. While comparing the corrugation individually, among the airfoils having single corrugation on the pressure side, airfoil-N1 has a smallest contribution of the shear drag to the total drag.

To investigate the effect of the angle of attack on the aerodynamic performance, a range of 0°–20° with 5° increment is selected. Figure 9 shows the variation of $\bar{C}_L$ and $\bar{C}_D$ with the angle of attack at Re = 1400. For the purpose of comparison, airfoils having single corrugation on the suction side and the pressure side are drawn separately. Another plot is drawn with airfoils SM, CR, M6, and N6. With an increase in the angle of attack, the lift and drag coefficients increase for all airfoils and no stalling is seen at Re = 1400. The slope of $\bar{C}_D$ is more steeper after 15° angle of attack. Comparing airfoils SM, CR, M6, and N6, airfoils SM and M6 have nearly the same lift up

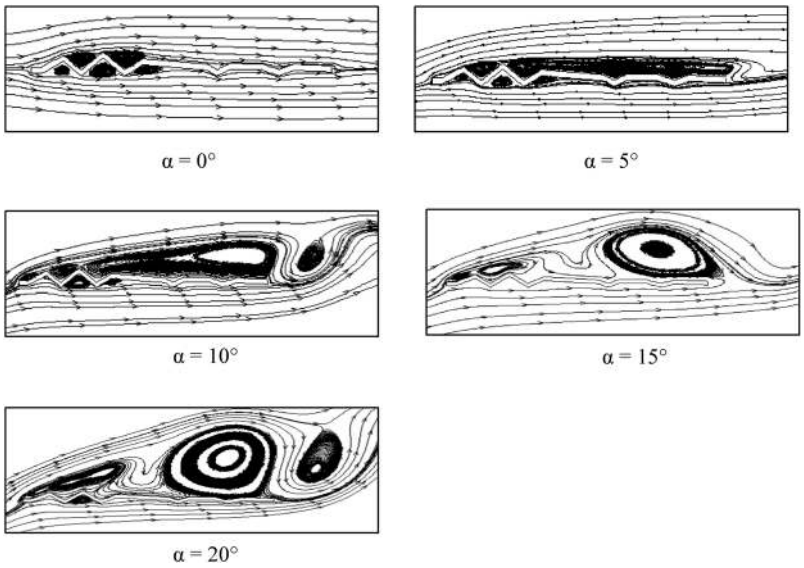

FIG. 11. Time averaged mean plot of the streamline at different angles of attack for airfoil-CR at Re = 1400.

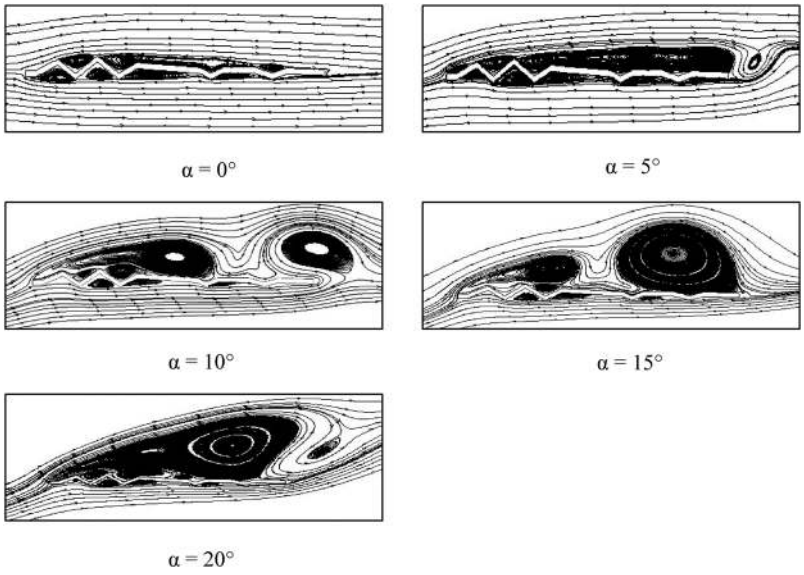

FIG. 12. Time averaged mean plot of the streamline at different angles of attack for airfoil-CR at Re = 6000.

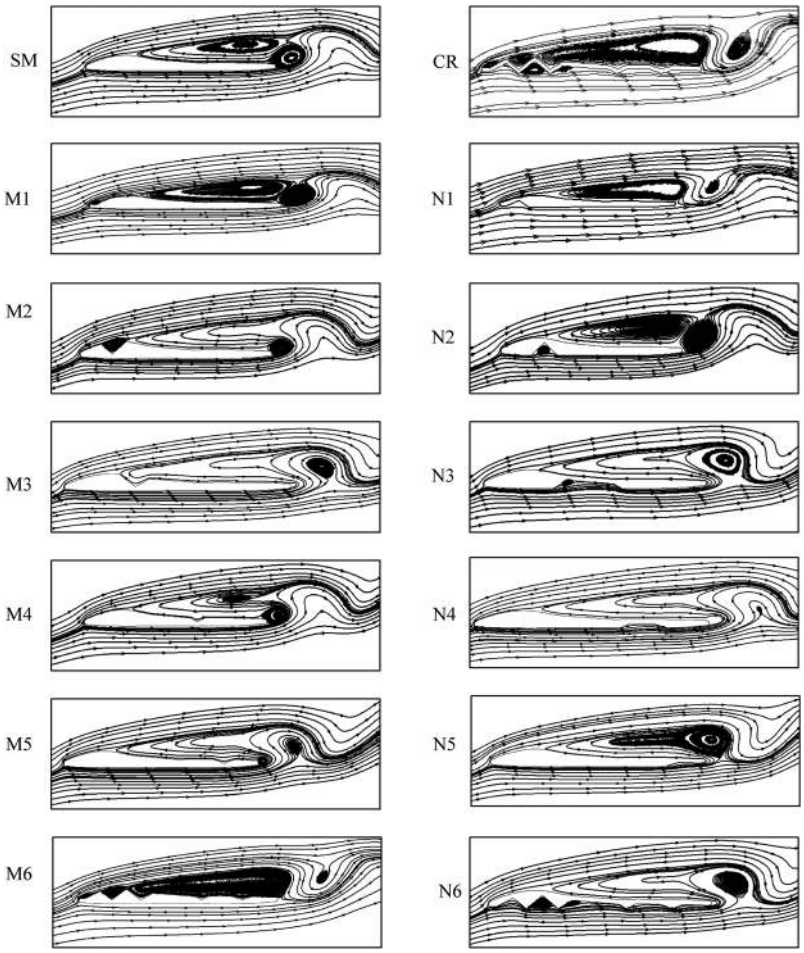

FIG. 13. Time averaged mean plot of the streamline at 10° for various airfoils at Re = 1400.

to 15° and CR and N6 up to 10°. At α = 20°, airfoil-M6 has the lowest lift and N6 has the highest lift among the airfoils. The drag coefficient is slightly higher beyond 10° for airfoil-CR. The lift and drag coefficient is about equal among airfoils (M1 to M5) at the corresponding angle of attack and similarly N1 to N5 have nearly similar values. As the angle of attack changes, lift and drag is unaffected by airfoil corrugation.

Figure 10 shows that the lift and drag coefficients for airfoil-CR, $\bar{C}_L$ increase with the angle of attack for Re = 150 and 1400, while for Re = 6000 and 10 000, the lift increases up to 20°

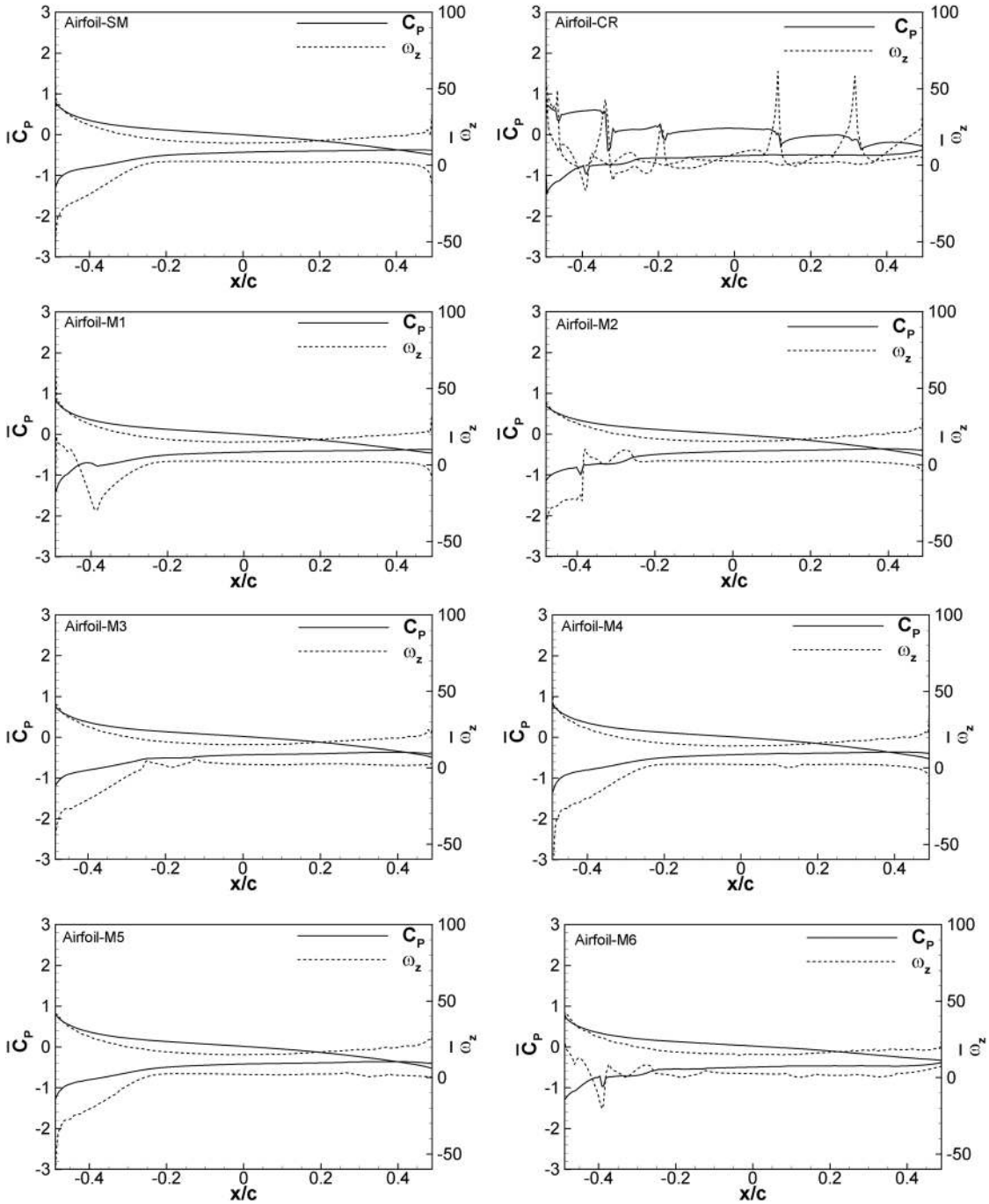

FIG. 14. Time averaged mean pressure coefficient on the surface of airfoil at 10° and Re = 1400.

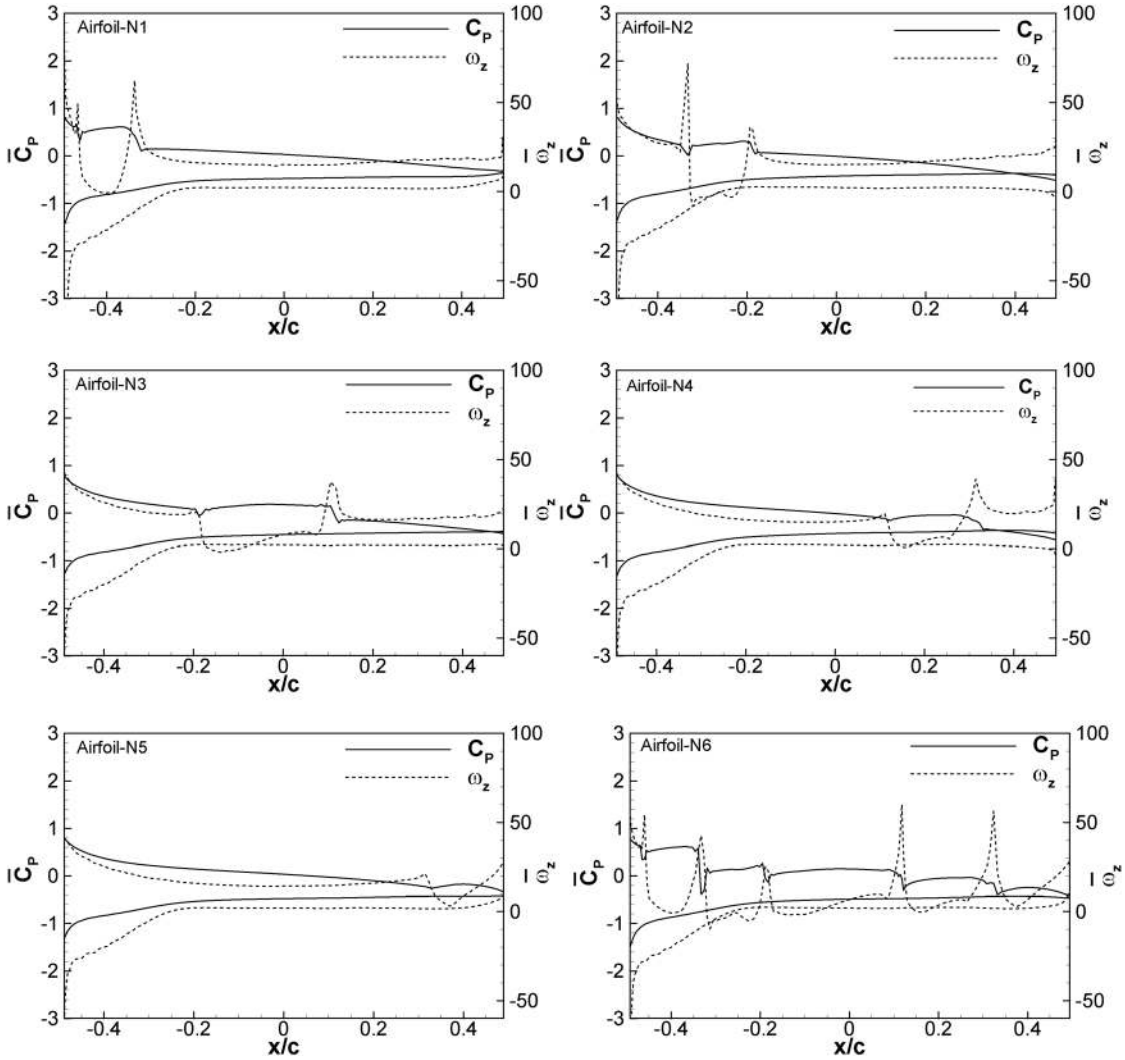

FIG. 14. *(Continued.)*

monotonically for Re = 150, while at other Re, it increases to a maximum and then decreases. The point of inflexion indicates stalling. However, the drag decreases as the Reynolds number is increased. As the angle of attack is increased, the drag converges to the same values for all Reynolds numbers. Time-averaged streamlines are shown for both Re = 1400 and 6000 in Figs. 11 and 12, respectively. Figure 11 indicates that, at 0° angle of attack, the flow is mostly attached to the surface of the airfoil and has trapped vortices in the corrugated valley near the leading edge, while for corrugation near the trailing edge, there is separation and reattachment of flow within the corrugation. As the angle is increased to 5°, the flow separates at the near leading edge and reattaches at the trailing edge. The size of the vortex increases, indicating the increasing vorticity on the surface of the airfoil. With a further increment in the angle of attack, the flow reattachment does not take place, and a large wake zone is shown where vortex shedding occurs. The time average streamlines shown in Fig. 12 depict that the flow is fully separated at 5°, but vortex shedding occurs only after 10° from the leading edge. The size of vortices rise up and split into two parts as the angle of attack is increased further. At 20°, a very thick layer of the vortex is formed on the upper surface.

C. Effect of corrugation

At Re = 1400, the maximum gliding ratio is found at 10° angle of attack, for which the time averaged streamline and mean pressure coefficient plot are shown in Figs. 13 and 14, respectively. The streamline pattern for airfoil-SM shows that there is a primary vortex near the trailing edge and on the upper surface near the trailing edge. The flow separation occurs through a small distance from the leading edge and backflow occurs from the trailing edge to the point

near the separation point. The airfoil M2 has slightly more distance attached to the airfoil. Airfoil-M6 has all the corrugation filled by vortices and flow separates at the leading edge. Airfoils M1 and M2 have trapped vortices, while M3, M4, and M5 have no such trapped vortices in the corrugations. A similar pattern is observed in airfoils having single corrugation on the suction side as the pressure side. The airfoils N1, N2, and N3 have trapped vortices in the corrugation. The size of the vortex in airfoils N1 and N3 is small as compared to N2.

The mean pressure coefficient and vorticity variation along its surface are shown in Fig. 14. It indicates that the corrugation on the suction side of airfoils has a slight influence on the pressure. The airfoil-M2 has a low-pressure peak near the corrugation due to which the pressure on the upper surface of the airfoil decreases; therefore, the lift enhances slightly. The vorticity near the region of corrugation on the pressure side of the airfoil decreases. The decrease in the velocity gradient $\partial u/\partial y$ is significant as compared to the velocity gradient $\partial v/\partial x$. Therefore, the vorticity $\bar{\omega}_z = \left[\left(\frac{\partial v}{\partial x}\right) - \left(\frac{\partial u}{\partial y}\right)\right]$ near the surface of the airfoil decreases due to the reduction of $\partial u/\partial y$. Therefore, a high pressure region is created near the corrugations on the pressure side of the airfoil. The main cause of enhancement in lift is due to the increase in the pressure on the lower surface of the airfoil due to corrugation. The size of the corrugation is large along the chordwise direction and has no trapped vortices for airfoils N3, N4, and N5 due to which a large region of high pressure is created on the lower surface of the airfoil as compared to airfoils N1 and N2, where the size of the corrugation is comparably small and has trapped vortices. Therefore, airfoils having corrugation near the trailing edge airfoils N3, N4, and N5 have higher lift coefficients as compared to corrugation near the leading edge airfoils N1 and N2.

The force coefficient data for all airfoils at Re = 1400 and angle of attack $\alpha = 10^\circ$ are tabulated in Table IV. Comparing the airfoils having single corrugation on the suction side, airfoil-M2 has the highest lift coefficient and gliding ratio when compared with airfoil-SM. The drag coefficient is nearly the same. Airfoil-N4 has the highest lift coefficient among the airfoil having single corrugation on the pressure side. From the above discussion, it is concluded that the corrugation near the leading edge for the suction side and corrugation near the trailing edge for the pressure side are advantageous for the aerodynamic performance. Comparing the airfoils SM, CR, M6, and N6, it is found that the lift coefficients for CR and N6 are nearly the same and about 16% higher than SM, while M6 has slightly lower $\bar{C}_L$ than SM. The gliding ratio is about 11% and 8% higher for N6 and CR, respectively, than SM. While M6 has 2.5% lower gliding performance as compared to SM. The reason for higher gliding performance for airfoil-N6 is the lower value of the drag coefficient in comparison with airfoil-CR. The corrugations of the airfoil CR also increase the pressure drag in comparison to the smooth surface. The drag coefficient is highest for CR among all airfoils and is 7.05% more in comparison to SM, and for airfoils N6 and M6, it is 3.85% and 1.92%, respectively, as compared to SM.

D. Gliding ratio

For gliding flight, the key quantity of interest is the gliding ratio which is the ratio of lift to drag. Figure 15 shows the comparison of the gliding ratio ($\bar{C}_L/\bar{C}_D$) with the angle of attack at different Reynolds numbers for various airfoil geometries. The angle at which the maximum $\bar{C}_L/\bar{C}_D$ ratio is achieved decreases with an increase in the Reynolds number. The maximum $\bar{C}_L/\bar{C}_D$ ratio is found at 15° and 10° angles of attack for Re = 150 and 1400, respectively. At Re = 6000, the angle at which maximum $\bar{C}_L/\bar{C}_D$ is found for airfoil CR and M6 is 5°, while for other airfoils, it is still at 10° and for Re = 10 000, the angle reduces to 5° for all airfoils. Table V shows the maximum $\bar{C}_L/\bar{C}_D$ and $\bar{C}_L$ with the corresponding angle

TABLE IV. Comparison of $C_{L_{min}}$, $C_{D_{min}}$, $C_{L_{max}}$, $C_{D_{max}}$, $\bar{C}_L$, $\bar{C}_D$, $\bar{C}_L/\bar{C}_D$, and period (T) time at 10° angle of attack and Re = 1400.

Re = 1400, α = 10°								
Airfoil	T	$C_{L_{min}}$	$C_{L_{max}}$	$C_{D_{min}}$	$C_{D_{max}}$	$\bar{C}_L$	$\bar{C}_D$	$\bar{C}_L/\bar{C}_D$
SM	0.966	0.497	0.604	0.150	0.161	0.549	0.156	3.532
CR	0.985	0.571	0.712	0.160	0.174	0.638	0.167	3.821
M1	0.969	0.495	0.605	0.151	0.162	0.549	0.156	3.512
M2	0.981	0.504	0.610	0.150	0.160	0.556	0.155	3.588
M3	1.022	0.492	0.606	0.150	0.161	0.548	0.155	3.525
M4	0.967	0.498	0.605	0.150	0.161	0.550	0.155	3.539
M5	0.989	0.494	0.609	0.151	0.161	0.550	0.156	3.528
M6	0.994	0.486	0.612	0.153	0.165	0.547	0.159	3.443
N1	0.988	0.503	0.613	0.150	0.161	0.557	0.155	3.586
N2	0.995	0.497	0.604	0.150	0.161	0.549	0.155	3.540
N3	0.969	0.514	0.621	0.151	0.163	0.567	0.157	3.609
N4	1.060	0.516	0.626	0.151	0.163	0.570	0.157	3.629
N5	0.954	0.514	0.622	0.151	0.161	0.567	0.156	3.628
N6	0.972	0.579	0.701	0.156	0.169	0.638	0.162	3.933

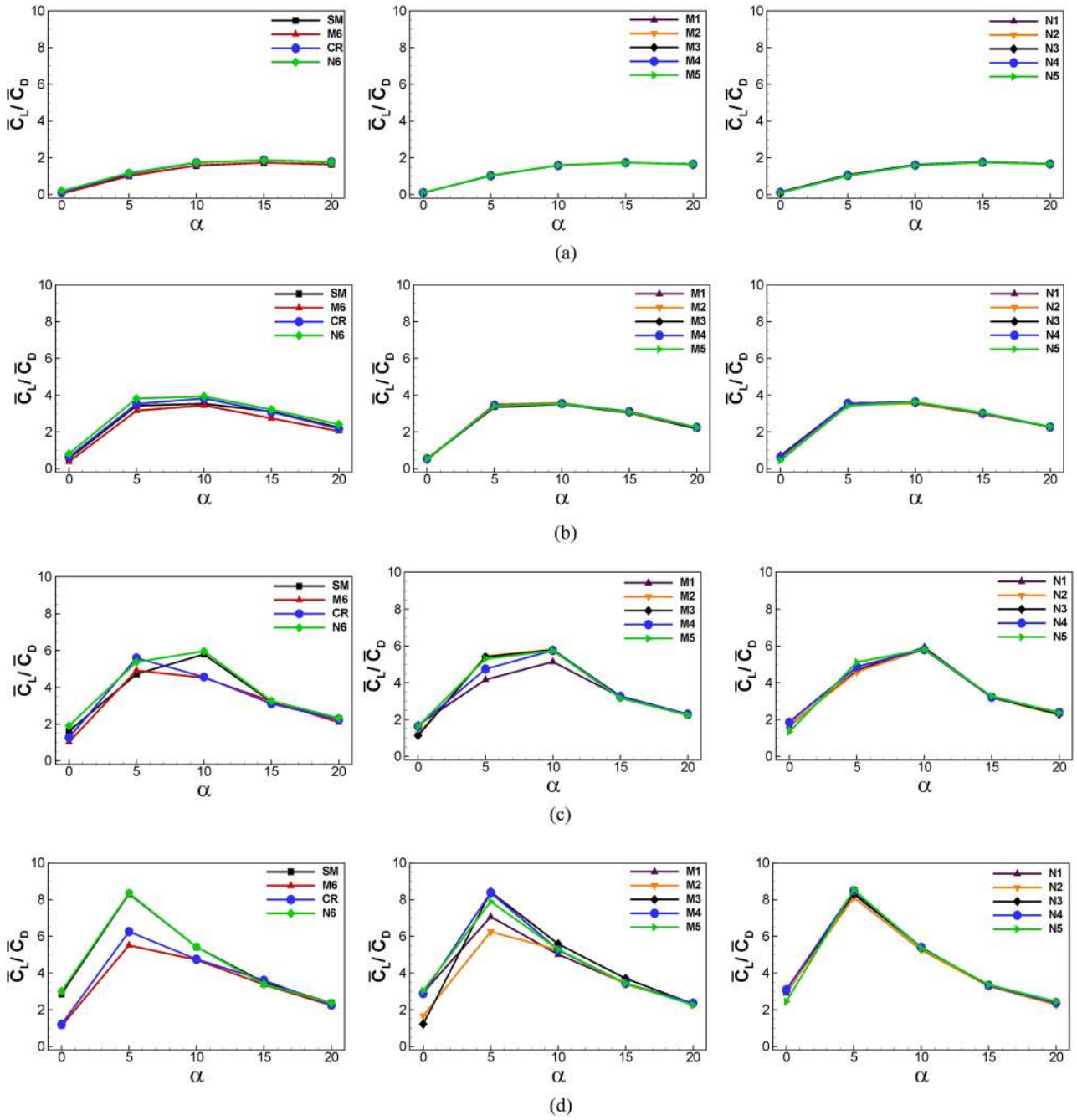

FIG. 15. Time averaged mean gliding ratio with the angle of attack for various airfoils at (a) Re = 150, (b) 1400, (c) 6000, and (d) 10 000.

of attack for various airfoils at different Reynolds numbers. The maximum gliding ratio of different airfoils is compared herein. At Re = 150 and 1400, for airfoils CR and SM, the $\bar{C}_L/\bar{C}_D$ for airfoil-CR is better than that for airfoil-SM. At Re = 6000 and 10 000, the $\bar{C}_L/\bar{C}_D$ performance for airfoil SM is greater as compared to airfoil-CR. The $\bar{C}_L/\bar{C}_D$ for M6 is nearly the same as for airfoil SM at Re = 150, but at other higher Reynolds numbers, the $\bar{C}_L/\bar{C}_D$ is not only lower than airfoil-SM but also from all the airfoils and it has 33.7% lower value as compared to SM at Re = 10 000. The performance of N6 is the same as CR at Re = 150 and SM at

TABLE V. Comparison of $(\bar{C}_L/\bar{C}_D)max$, and $(\bar{C}_L)max$ and the corresponding angle of attack (given in bracket), at Re = 150, Re = 1400, Re = 6000, and Re =10 000.

	Re = 150		Re = 1400		Re = 6000		Re = 10 000	
Airfoil	$(\bar{C}_L/\bar{C}_D)max$	$(\bar{C}_L)max$	$(\bar{C}_L/\bar{C}_D)max$	$(\bar{C}_L)max$	$(\bar{C}_L/\bar{C}_D)max$	$(\bar{C}_L)max$	$(\bar{C}_L/\bar{C}_D)max$	$(\bar{C}_L)max$
SM	1.7321 (15°)	0.7602 (20°)	3.5324 (10°)	0.9676 (20°)	5.7932 (10°)	1.1765 (15°)	8.3182 (5°)	1.3046 (15°)
CR	1.8722 (15°)	0.8246 (20°)	3.8211 (10°)	1.0098 (20°)	5.6005 (5°)	1.1603 (15°)	6.2557 (5°)	1.3033 (15°)
M6	1.7344 (15°)	0.7507 (20°)	3.4435 (10°)	0.8946 (20°)	4.9154 (5°)	1.1320 (15°)	5.5123 (5°)	1.1769 (15°)
N6	1.8728 (15°)	0.8166 (20°)	3.9330 (10°)	1.0584 (20°)	5.9651 (10°)	1.1364 (15°)	8.3519 (5°)	1.2118 (15°)
M1	1.7354 (15°)	0.7579 (20°)	3.5124 (10°)	0.9540 (20°)	5.1365 (10°)	1.1455 (15°)	7.0636 (5°)	1.2968 (15°)
M2	1.7419 (15°)	0.7547 (20°)	3.5878 (10°)	0.9467 (20°)	5.8139 (10°)	1.1774 (20°)	6.2491 (5°)	1.1745 (15°)
M3	1.7276 (15°)	0.7614 (20°)	3.5251 (10°)	0.9437 (20°)	5.7849 (10°)	1.0380 (15°)	8.4210 (5°)	1.1898 (15°)
M4	1.7313 (15°)	0.7595 (20°)	3.5386 (10°)	0.9667 (20°)	5.7555 (10°)	1.2002 (15°)	8.3773 (5°)	1.2851 (15°)
M5	1.7297 (15°)	0.7585 (20°)	3.5283 (10°)	0.9437 (20°)	5.7428 (10°)	1.0222 (15°)	7.8906 (5°)	1.1695 (15°)
N1	1.7498 (15°)	0.7598 (20°)	3.5860 (10°)	0.9463 (20°)	5.9241 (10°)	1.0507 (15°)	8.3825 (5°)	1.1451 (15°)
N2	1.7425 (15°)	0.7580 (20°)	3.5403 (10°)	0.9472 (20°)	5.8090 (10°)	1.0294 (15°)	8.1114 (5°)	1.1477 (15°)
N3	1.7671 (15°)	0.7746 (20°)	3.6094 (10°)	0.9819 (20°)	5.8386 (10°)	1.1996 (15°)	8.3036 (5°)	1.2849 (15°)
N4	1.7538 (15°)	0.7676 (20°)	3.6290 (10°)	0.9828 (20°)	5.8016 (10°)	1.2078 (15°)	8.4880 (5°)	1.3083 (15°)
N5	1.7418 (15°)	0.7638 (20°)	3.6278 (10°)	0.9991 (20°)	5.8179 (10°)	1.2376 (15°)	8.5377 (5°)	1.3430 (15°)

Re = 10 000, while at Re = 1400 and 6000, its performance is better with both airfoils. The $\bar{C}_L/\bar{C}_D$ for airfoil N6 is 11.33% and 2.94% higher as compared to SM at Re = 1400 and 6000, respectively. The airfoil-M2 has slightly higher $\bar{C}_L/\bar{C}_D$ up to Re = 6000, but at Re = 10 000, the performance is poor among the single corrugated airfoil on the suction side and is equal to airfoil-CR. The airfoils having single corrugation on the pressure side have about the same performance among them, and the performance is not more than 3% in comparison to airfoil-SM. From the above discussion, it is found that the maximum value of $\bar{C}_L/\bar{C}_D$ is obtained at a smaller angle of attack as the Reynolds number is increased. Airfoil CR performance is better as compared to SM at low Reynolds numbers 150 and 1400. Airfoil SM performance is improved as compared to airfoil CR at higher Reynolds numbers 6000 and 10 000. Single corrugated airfoils have very slight variation in performance among them. Airfoil-N6 performs best at all considered Reynolds numbers.

E. Effect of Reynolds number

Reynolds number is an important parameter to determine the performance of the wing. To check the effect of Re, an intermediate angle of attack $\alpha = 10^\circ$ is selected, where the highest gliding ratio is found at Re = 1400 and also the actual gliding for the dragonfly occurs at around this Reynolds number (Kim *et al.*, 2009). The effect of Reynolds number is studied for maximum gliding ratio $\bar{C}_L/\bar{C}_D$, and the aerodynamic performance of various airfoils is compared. Figure 16 shows the time-averaged streamline at 10° angle of attack for CR, SM, M6, and N6 airfoils. Taking 50 cycles, time-averaged flows were obtained. Figure 16 shows that, at Re = 150, the flow is fully attached to the surface of airfoil-SM, while other airfoils have trapped vortices in the corrugated valley near the leading edge on the suction side of the airfoil. Flow separation and reattachment occur within or near the edge of the corrugated valley of the wing. At higher Reynolds numbers, there exists a large region of separation over the upper surface of the airfoil. The airfoils CR and M6 have fully separated flows, while airfoils SM and N6 have a separated region starting from the distance 0.25c from the leading edge at Re = 1400. As the Reynolds number increases to 6000, the primary vortex on the upper surface of the airfoil splits into several secondary flow vortices all over the surface of the airfoil. These secondary vortices move toward the leading edge of the airfoil at Re = 10 000 and the separation region increases.

Figure 17 shows the comparison of the time-averaged force coefficient and gliding ratio with varying Reynolds numbers at 10° angle of attack. At Re = 150, the highest value of $\bar{C}_L$ and $\bar{C}_L/\bar{C}_D$ is found for airfoil-N6. As the Reynolds number increases from 150 to 1400, the lift coefficient slightly increases for airfoils CR, N5, and N6. For the other airfoils, the lift coefficient slightly decreased. On the other hand, for all airfoils, there is a larger decrease in the drag coefficient due to which the gliding ratio is increased. The highest value of $\bar{C}_L$ is 0.638, which is the same for airfoils N6 and CR, but airfoil CR has a higher drag as compared to N6. Therefore, again N6 becomes the best performing airfoil. There is a rapid increase in the lift coefficient as the Reynolds number changes from 1400 to 6000. The lowest value of $\bar{C}_L$ at Re = 6000 is 0.89 for M6 and highest 1.08 for N6. The drag coefficient also increased as Re is increased. The largest $\bar{C}_D$ value is 0.214 for CR and lowest for N1 have value 0.170. The increase in $\bar{C}_L/\bar{C}_D$ is due to the rise in the lift coefficient. The highest value is 5.96 for N6 and the lowest is 4.52 for M6 followed by CR, which is 4.56, while for SM is 5.79. The largest $\bar{C}_L$ and $\bar{C}_L/\bar{C}_D$ are found in the case of airfoil-N6. There is a small variation as the Reynolds number increased from 6000 to 10 000. The largest $\bar{C}_L$ is 1.10 for airfoil N5. The $\bar{C}_L/\bar{C}_D$ ratio is slightly larger for M6 and CR, while other airfoils have decreased values. The airfoils having highest $\bar{C}_L/\bar{C}_D$ are 5.59 for M3 and 5.43 for N6. For other airfoils, $\bar{C}_L/\bar{C}_D$ is 4.72 for M6, 4.75 for CR, and 5.4 for airfoil SM. It can be concluded that there is a slight change in the lift coefficient as the Reynolds number increases from 150 to 1400. The increase in $\bar{C}_L/\bar{C}_D$ is due to a steep decrease in the drag coefficient. In this range of Reynolds

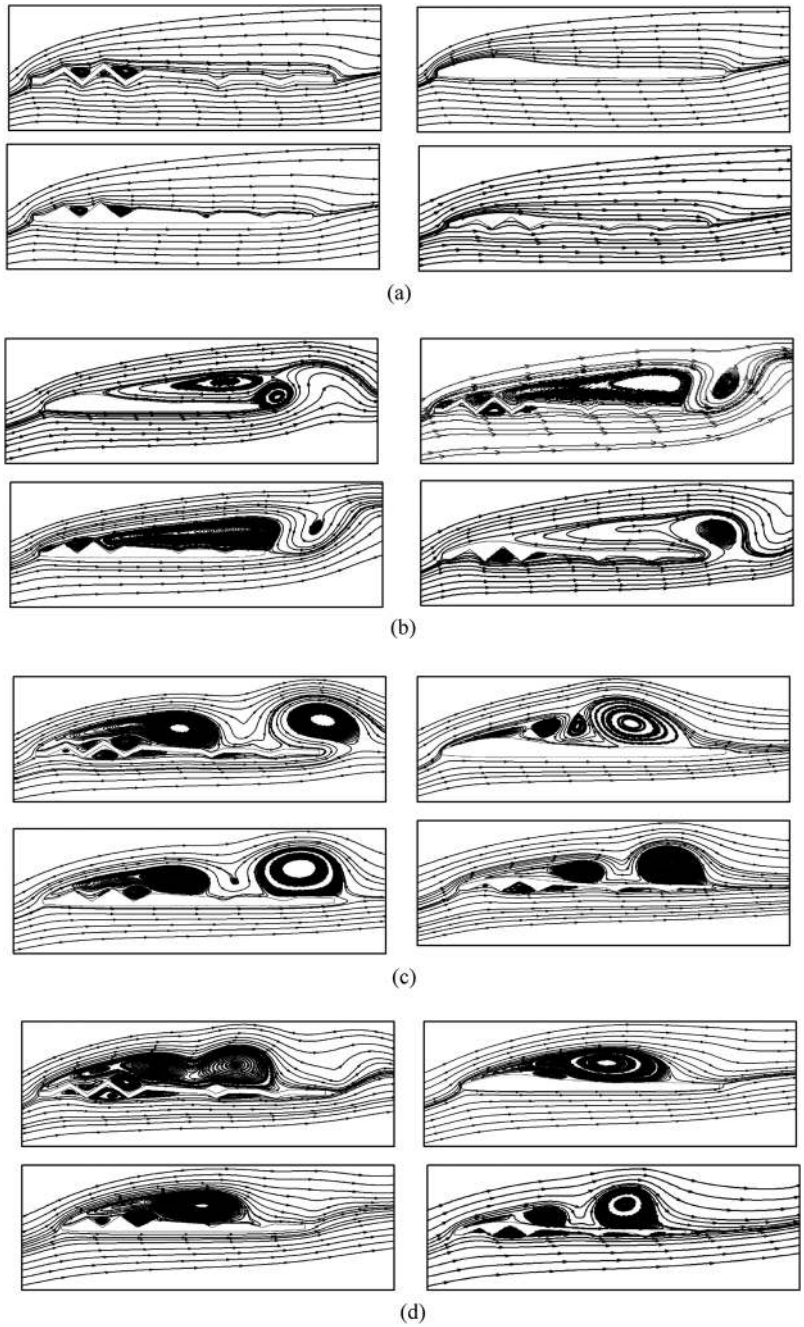

FIG. 16. Time averaged streamline plot for airfoils-CR, SM, M6, and N6 at 10° angle of attack for (a) Re = 150, (b) Re = 1400, (c) Re = 6000, and (d) Re = 10 000.

numbers (150–1400), the higher gliding ratio is obtained due to a decrease in the drag coefficient. As the Reynolds number changes from 1400 to 6000, the increase in the lift coefficient is more as compared to the decrease in the drag coefficient; therefore, the rise in the lift coefficient has a greater fraction for a higher value of $\bar{C}_L/\bar{C}_D$. The change in the force coefficient is not significant when the Reynolds number increases from 6000 to 10 000. The best performing airfoil is N6 at Re = 150, 1400, and 6000, while at Re = 10 000, the $\bar{C}_L/\bar{C}_D$ is the second highest for N6, while the largest value of gliding ratio is found for M3.

F. Optimization

Since the airfoils have different performances at various angles of attack and Reynolds numbers, it is essential to find out the optimized, both in terms of the shape of the airfoil as well as the angle

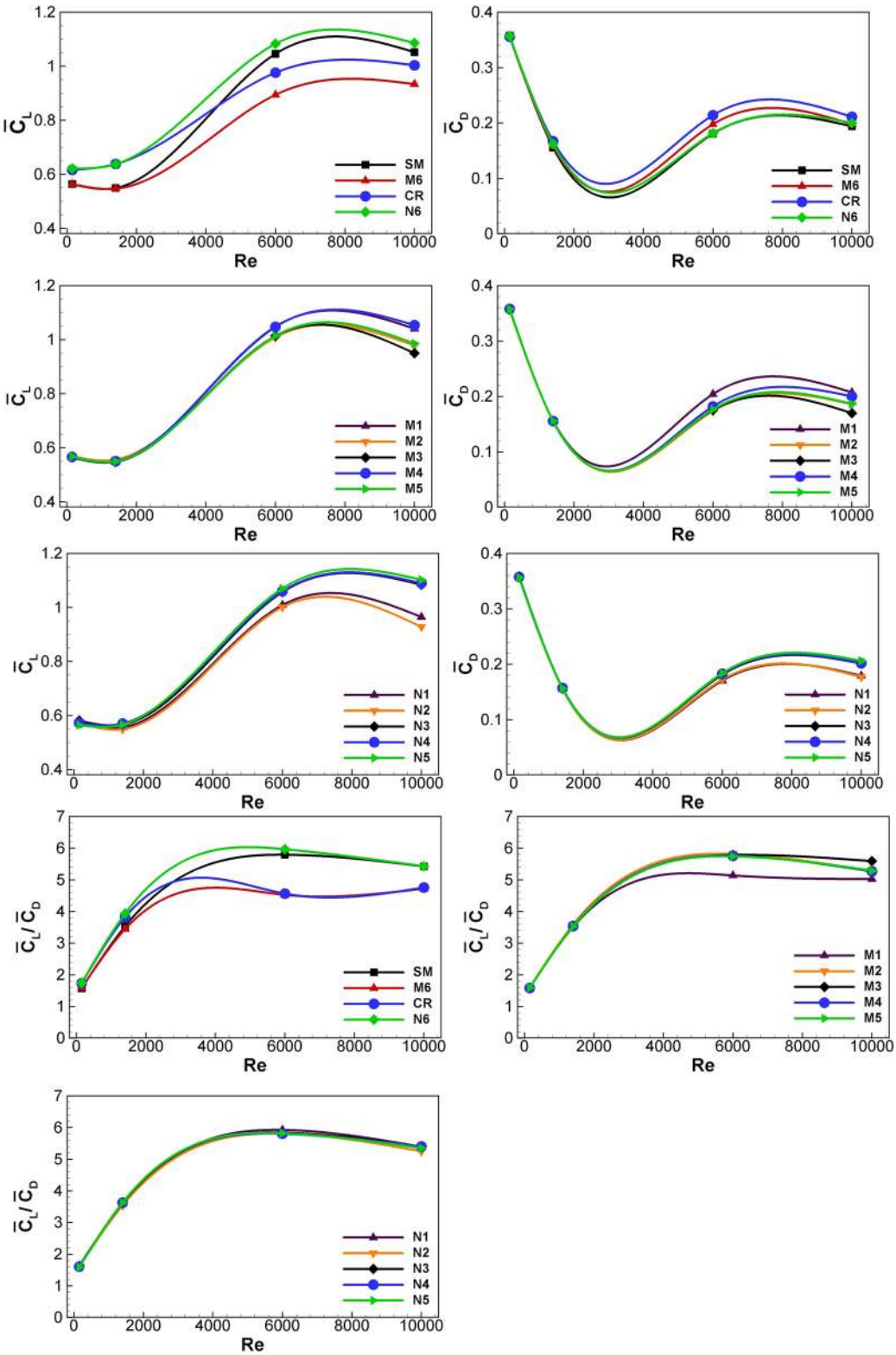

FIG. 17. Variation of the time averaged mean lift and drag coefficient and gliding ratio with Reynolds number at 10° angle of attack for various airfoils.

TABLE VI. Weights of RBNN, RSA, and KRG surrogates to construct weighted average surrogates.

Reynolds number (Re)	RBNN	RSA	KRG
150	0.224	0.331	0.445
1400	0.405	0.228	0.337
6000	0.357	0.289	0.354
10 000	0.402	0.306	0.292

TABLE VII. Comparison of optimal values of airfoil and angle of attack for maximum values of $(\bar{C}_L/\bar{C}_D)_{max}$, at Re = 150, Re = 1400, Re = 6000, and Re = 10 000.

		Surrogate model	Surrogate model	CFD		
Re	Airfoil	α (deg)	$\bar{C}_L/\bar{C}_D$	$\bar{C}_L$	$\bar{C}_D$	$\bar{C}_L/\bar{C}_D$
150	N6	14.83	1.908	0.77	0.405	1.901
150	CR	14.83	1.908	0.77	0.405	1.901
1400	N6	9.97	3.901	0.64	0.162	3.936
6000	N5	9.22	6.095	1.08	0.164	6.569
10 000	N3	5.276	8.597	0.75	0.081	9.178

of attack together, for which higher performance is achieved at a particular Reynolds number. For this purpose, $\bar{C}_L/\bar{C}_D$ is maximized as a single objective function by taking the shape of the airfoil and the angle of attack as design parameters.

The surrogate-based optimization technique is applied to find the optimum value of the angle of attack (α) and the shape of airfoil having a highest value of $\bar{C}_L/\bar{C}_D$. After validation of the numerical solver and data obtained from the CFD results, design of experiment (DOE) is created. In this step, the range of design space is identified for the design variables selected. A total of 70 sample designs were created within the design space assuming other design parameters constant.

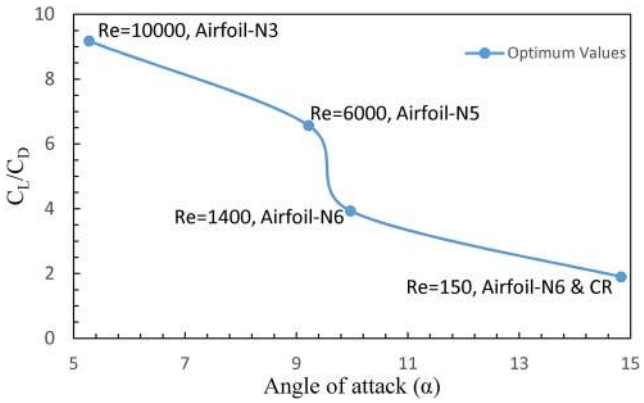

FIG. 18. Time averaged mean gliding ratio with the optimum angle of attack for various airfoils at Re = 150, 1400, 6000, and 10 000.

The surrogate of the average weight of Kriging, response surface approximation, and radial based neural network model is used. The weight found for different models to construct a weighted average surrogate is tabulated in Table VI. The optimized airfoil at different Reynolds numbers are again run for CFD simulation at the corresponding optimized angle of attack to find the force coefficient and gliding ratio is tabulated in Table VII. At Re = 150, airfoils CR and N6 have the maximum value of $\bar{C}_L/\bar{C}_D$.

At optimum condition for flight Reynolds number, $\bar{C}_L/\bar{C}_D$ is the highest for that particular airfoil and angle of attack. The gliding

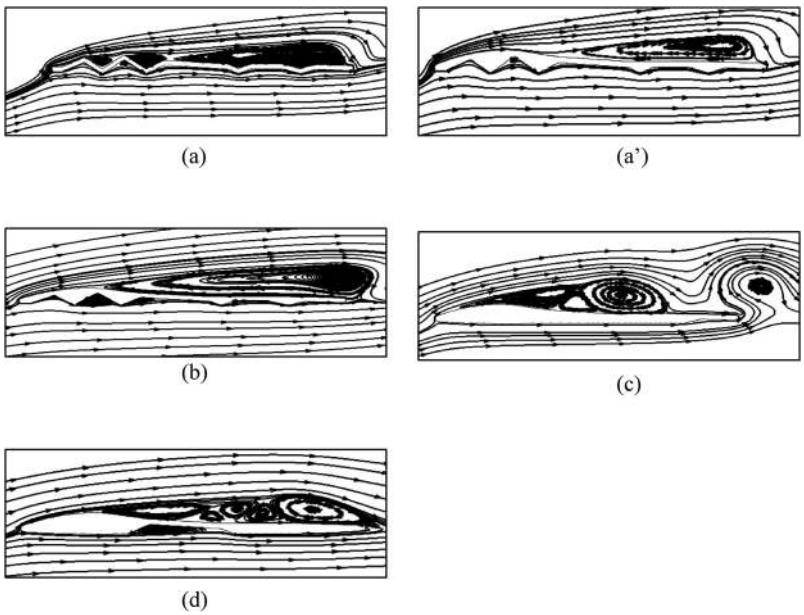

FIG. 19. Time averaged streamline plot for optimal airfoils and angle of attack (α) having maximum value of $\bar{C}_L/\bar{C}_D$ at various Reynolds numbers (a) Re = 150, α = 14.83°, CR; (a′) Re = 150, α = 14.83°, N6; (b) Re = 1400, α = 9.97°, N6; (c) Re = 6000, α = 9.22°, N5; and (d) Re = 10 000, α = 5.276°, N3.

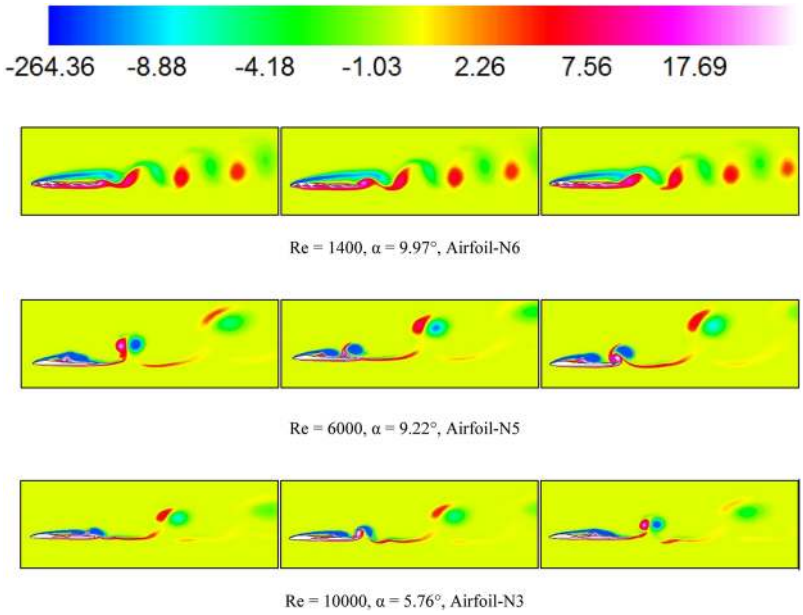

FIG. 20. Vorticity contour plot at different time instants and Re = 1400, 6000, and 10 000 for optimum conditions.

ratio $\bar{C}_L/\bar{C}_D$ is plotted for an optimum value of angle of attack α at the corresponding Reynolds number, and an optimum airfoil shape is shown in Fig. 18. The optimum values of angle of attack are large for low Reynolds numbers and small for high Reynolds numbers.

Figure 19 shows the streamlines at optimum conditions at various Reynolds numbers. At Re = 150, the optimum value of the angle of attack α = 14.83° and airfoils CR and N6 have similar performance in terms of the gliding ratio. It shows that at an ultralow Reynolds number, cavity of corrugation on the upper surface is filled with trapped vortices and the fully corrugated upper surface behaves like a smooth surface. The upper surface corrugation has little impact on the performance. The flow separates and reattaches near the trailing edge on the upper surface for both airfoils CR and N6. On the other hand, at the lower surface, separation and reattachment of flow occurs within the corrugation. But as the Reynolds number increases to 1400, the gliding ratio becomes 2.08 times as compared to

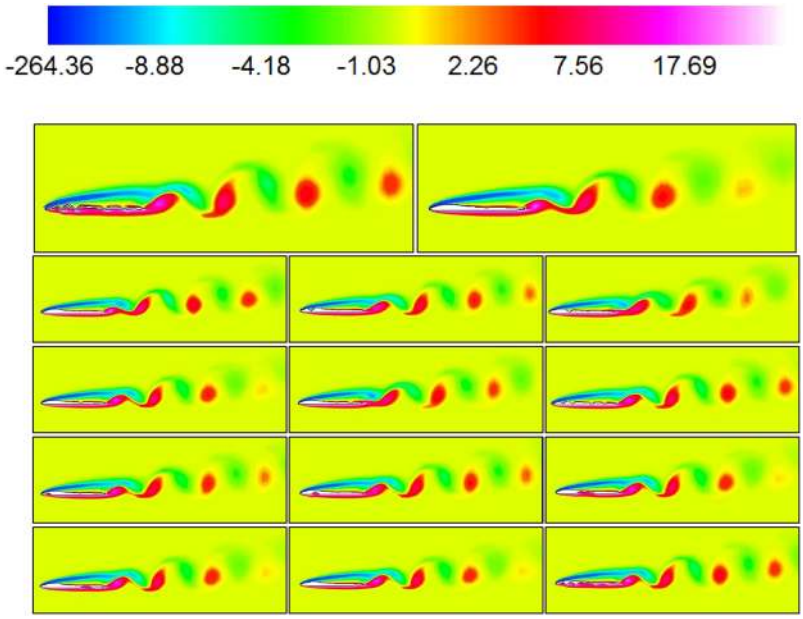

FIG. 21. Instantaneous vorticity contour plot at α = 10° and Re = 1400 for various airfoils.

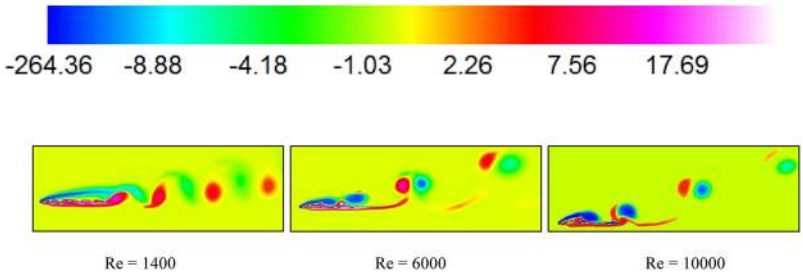

FIG. 22. Vorticity contour plot at angle of attack 10° and Re = 1400, 6000, and 10 000 for airfoil-CR.

Re = 150. The optimum angle of attack α becomes 9.97° having $\bar{C}_L/\bar{C}_D$ = 3.936 for the corresponding optimum airfoil N6, and the strength and extent of the separation zone of vortex formation on the upper surface increases. The airfoil having the upper surface smooth and lower corrugated N6 has better performance as compared to both side corrugated airfoil-CR. At Re = 6000 and 10 000, the gliding ratio becomes 3.46 and 4.82 times $\bar{C}_L/\bar{C}_D$ at Re = 150, respectively. At Re = 6000, the upper surface vortex is split into three vortices for the optimum airfoil-N5 at an optimum angle of attack α = 9.22° and the number of splits of the vortex increases at Re = 10 000 in the separation for which the optimum value of the angle of attack α is 5.276° and airfoil-N3. The optimum value of the angle of attack is the angle

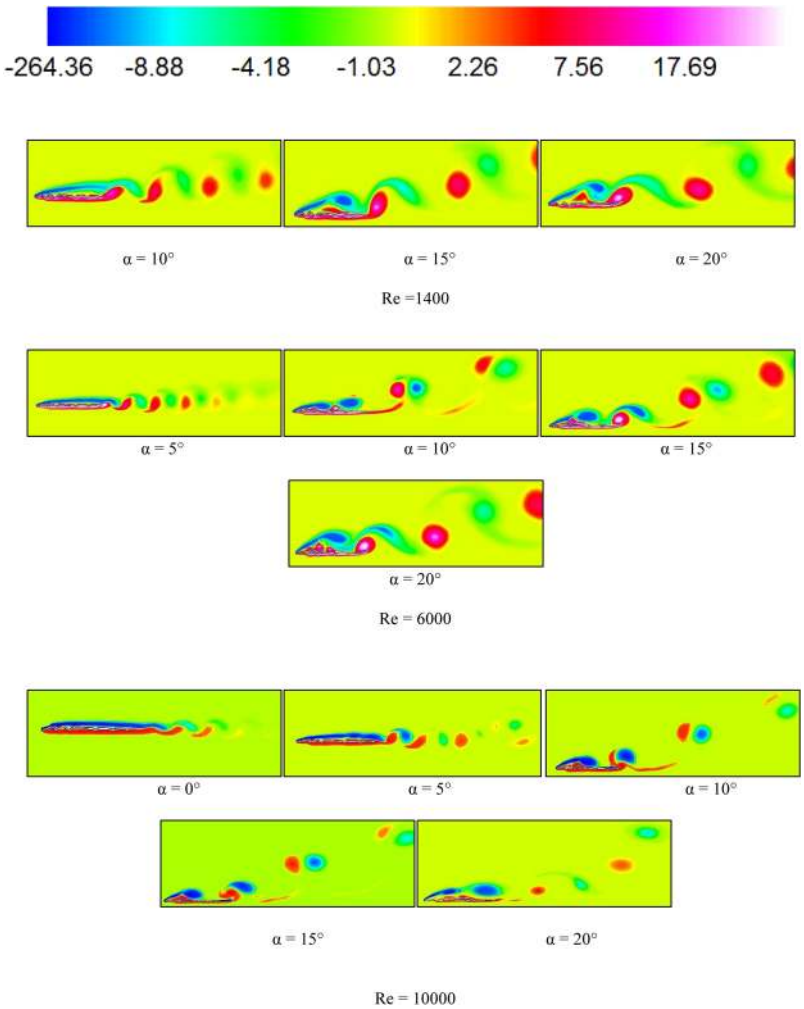

FIG. 23. Vorticity contour plot at different angles of attack and Re = 1400, 6000, and 10 000 for airfoil-CR.

at which the $\bar{C}_L/\bar{C}_D$ is highest, and if the angle of attack increases or decreases, the ratio $\bar{C}_L/\bar{C}_D$ decreases.

Figure 20 shows the vorticity plot at three different time instants for different Reynolds numbers. For the analysis, an optimum airfoil and the corresponding optimum angle of attack are considered at that Reynolds number. At Re = 1400, the vorticity plot for airfoil-N6 and α = 9.97 shows that the clockwise vortex sheds from the leading edge and collides with the vortex at the trailing edge at a small distance from the trailing edge in the wake region due to which the trailing edge vortex detached from the trailing edge, while due to the rise in the size of the trailing edge vortex, the leading edge vortex detached and shed into the wake. At Re = 6000, the vorticity plot for airfoil-N5 and α = 9.22° shows that as the trailing edge vortex is shed, the leading edge vortex moves from the leading edge to near the trailing edge and detaches itself from the continuous vortex from the leading edge in the mid upper surface of the airfoil and finally shedding occurs. The wake rolls back on the upper surface of the airfoil and merges with the counterclockwise vortex on the surface and then sheds it. Similar vortex shedding is achieved at Re = 10 000 for airfoil-N3, and α = 5.76° shows that there is also the same pattern as in the case Re = 6000.

G. Wake dynamics

Vorticity contour plots are drawn to understand the structures and wake formed at various Reynolds numbers. In these vorticity plots, red and blue contours represent the counterclockwise and clockwise vorticity, respectively, and various observations are found. Figure 21 shows the vorticity plot for different airfoils at 10° angle of attack and Re = 1400. It can be seen that the vorticity contour near the airfoil and in the wake region has the same pattern for all airfoils. The vortex shedding occurs from both the leading edge and trailing edge. On the lower surface of the airfoil, the vortex is fully attached to the surface, while on the upper surface, the vortex sheds from the leading edge and collides with the trailing edge vortex and both vortices are shed.

Figure 22 shows the vorticity contours for airfoil-CR at 10° and Re = 1400, 6000, and 10 000. At Re = 1400, the vortex is shed from both the leading edge and trailing edge. The wake for all airfoils is organized like a von Karman vortex street. At Re = 6000, both clockwise and counterclockwise vortices were formed on the leading edge, while the clockwise vortex was formed on the trailing edge. The clockwise vortex reattaches to the airfoil in the middle and before shedding in the wake, it interacts with the vortex from the trailing edge, whereas the counter clockwise vortex moves near the trailing edge and combines with the counterclockwise vortex from the trailing edge. It is attached to the surface for a distance by a striplike structure before shedding in the wake. As the angle of attack increased, the wake is still organized as von Karman street. However, as the Re is increased, von Karman organized street is destroyed and the vortex was shed from the trailing edge as doublets as shown in Fig. 23. Figure 23 shows the vorticity contours at different angles of attack and Reynolds numbers. At Re = 1400, angles of attack are 10°, 15°, and 20°, where vortex shedding occurs. The size of the vortex increases with an increase in the angle of attack, and in addition, there is counterclockwise formation of the vortex in the middle of the airfoil which merges with the trailing edge vortex before shedding in the wake. At Re = 6000, 5°, 10°, 15°, and 20° angles of attack, vortex shedding occurs. The vortex shedding pattern is similar to that at Re = 1400 and 10° angle, but the size of the vortex is small. While at a higher angle, the leading edge vortex again reattaches to the surface of the airfoil before shedding. The counterclockwise vortex sheds with a small striplike structure attached to it. At 20° angle, the size of the shedding vortex structure is large, but not striplike structure attached and the counterclockwise vortex occupies a large area on the surface of the airfoil. At Re = 10 000, shedding occurs at all angles between 0° and 20°. At 0°, shedding occurs alternately at both leading and trailing edge vortices, near the trailing edge into the wake. The size of the vortex increases at 5°. The striplike structure forms after shedding the counter clockwise vortex, which gets attached to it before finally shedding into the wake. At 15° and 20°, the structure becomes complicated, as the counterclockwise vortex formed on the large area of the airfoil and the trailing edge vortex rolls back on the upper surface of the airfoil before shedding.

VI. CONCLUSION

The numerical analysis of the dragonfly in the gliding mode for different corrugations on the surface of the wing is carried out for Re = 150, 1400, 6000, and 10 000. It was successfully demonstrated that the position and presence of corrugation affects the nature of flow and aerodynamic performance. At Re = 10 000 and angle of attack α = 0°, the transient nature of the flow is also affected by corrugation. The flow is oscillatory for airfoils CR, M1, M2, M3, M5, M6, N1, and N2, while steady for SM, M4, N3, N4, N5, and N6. The nature of the flow changes with an increase in the angle of attack and Reynolds number.

The lowest shear drag was found for a fully corrugated airfoil (CR) as these corrugations have trapped vortices near leading so the corrugation near the leading edge airfoils M2 and N1 has the lowest shear drag among a single corrugated airfoil. However, the total drag is also found to be highest in the corrugated airfoil CR as the pressure drag relatively increases as compared to the smooth airfoil. Therefore, it can be observed that corrugations near the leading edge decrease the shear drag without changing the pressure drag; hence, the total drag is reduced.

The suction side (upper surface) corrugation has little influence on the pressure, while the pressure side (lower surface) corrugation creates high pressure regions; therefore, the pressure on the lower surface increases, which is the main cause for the increase in the lift coefficient.

At Re = 1400 and 10° angle of attack, $\bar{C}_L/\bar{C}_D$ is highest for airfoil-N6. Airfoil-M2 has the highest lift coefficient among airfoils having single corrugation on suction. However, airfoil-M6 has lowest $\bar{C}_L$ and $\bar{C}_L/\bar{C}_D$ among all airfoils or say that it exhibits poor performance.

Comparing the fully corrugated airfoil CR with the smooth airfoil SM, the performance of CR is better than SM at low Reynolds numbers (150 and 1400) and SM is better than CR at high Reynolds numbers (6000 and 10 000).

The airfoil-N6 has aerodynamic performance nearly equal to airfoil-CR at low Reynolds numbers and slightly better at high Reynolds numbers as compared to airfoil-SM. Therefore, it is finally concluded that airfoil-N6 has better performance at all Reynolds numbers.

For a maximum gliding ratio, the optimum shape and angle of attack are determined from the weighted surrogate optimization technique and then validated from numerical simulations that found that the Reynolds number affects the shape and angle of attack. An airfoil having full corrugation on both (lower and upper) surfaces (CR) and full corrugation on the lower surface (N6) are the optimum shape having highest $\bar{C}_L/\bar{C}_D$ for Re = 150 at optimum angle $\alpha = 14.83°$. Airfoils having full corrugation on the lower surface (N6), corrugation near the trailing edge on the lower surface (N5), and corrugation in the middle on the lower surface (N3) are optimum airfoil shapes having the highest value of $\bar{C}_L/\bar{C}_D$ at angles of attack $\alpha = 9.97°$, 9.22°, and 5.276° for Re = 1400, 6000, and 10 000, respectively.

REFERENCES

Alexander, D. E., "Unusual phase relationships between the forewing and hind wings in flying dragonflies," J. Exp. Biol. **109**, 379–383 (1984).

Armfield, S. and Street, R., "The fractional-step method for the Navier–Stokes equations on staggered grids: The accuracy of three variations," J. Comput. Phys. **153**(2), 660–665 (1999).

Bose, C. and Sarkar, S., "Investigating chaotic wake dynamics past a flapping airfoil and the role of vortex interactions behind the chaotic transition," Phys. Fluids **30**, 047101-1 (2018).

Brodsky, A., "The aerodynamics of insect flight," in *The Evolution of Insect Flight* (Oxford University Press, New York, 1994).

Chorin, A. J., "Numerical solution of the Navier–Stokes equations," Math. Comput. **22**(104), 745–762 (1968).

Deb, K., "Single and multi-objective optimization using evolutionary computation," in Proceedings of the 6th International Conference on Hydroinformatics, Singapore, 2004.

Dukowwicz, J. K. and Dvinsky, A. S., "Approximate factorization as a high-order splitting for the implicit incompressible flow equations," J. Comput. Phys. **102**(2), 336–347 (1992).

Ennos, A. R., "The effect on the optimal shapes of gliding insect and seeds," J. Zool. **219**, 61–69 (1989).

Glaz, H. M., Bell, J. B., and Colella, P., "A second-order projection method for the incompressible Navier-Stokes equations," J. Comput. Phys. **85**(2), 257–283 (1989).

Goel, T., Raphael, T. H., Wei, S., and Nestor, V. Q., "Ensemble of surrogates," Struct. Multidiscip. Optim. **33**(3), 199–216 (2007).

Han, J.-S., Kim, H.-Y., and Han, J.-H., "Interactions of the wakes of two flapping wings in hover," Phys. Fluids **31**, 021901-1 (2019).

Hankin, E. H., "The soaring flight of dragonflies," Proc. Cambridge Philos. Soc. **20**, 460–465 (1921).

Hu, H. and Tamai, M., "Bioinspired corrugated airfoil at low Reynolds numbers," J. Aircr. **45**(6), 2068–2077 (2008).

Murphy, J. T. and Hu, H., "An experimental study of a bio-inspired corrugated airfoil for micro air vehicle applications," Exp. Fluids **49**(2), 531–546 (2010).

Kesel, A. B., "Aerodynamic characteristics of dragonfly wing sections compared with technical aerofoils," J. Exp. Biol. **203**, 3125–3135 (2000).

Kim, W. K., Ko, J. H., Park, H. C., and Byun, D., "Effect of corrugation of the dragonfly wing on gliding performance," J. Theor. Biol. **260**, 523–530 (2009).

Kunz, P. J. and Kroo, H., "Analysis and design of airfoils for use at ultra-low Reynolds numbers," in *Fixed and Flapping Wing Aerodynamics for Micro Air Vehicles Applications*, edited by Mueller, T. J. (AIAA, Virginia, 2001), Vol. 195, pp. 35–60.

Lee, S. H. and Kim, D., "Aerodynamics of a translating comb-like plate inspired by a fairyfly wing," Phys. Fluids **29**, 081902-1 (2017).

Lee, S. H., Lahooti, M., and Kim, D., "Aerodynamic characteristics of unsteady gap flow in a bristled wing," Phys. Fluids **30**, 071901-1 (2018).

May, M. L., "Thermal adaptation to temperature in dragonflies," Odonatologica **7**, 27–47 (1978).

May, M. L., "Dependence of flight behavior and heat production on air temperature in the green darner dragonfly Anax junius (Odonata: Aeshnidae)," J. Exp. Biol. **198**, 2385–2392 (1995).

McCall, J., "Genetic algorithms for modelling and optimisation," J. Comput. Appl. Math. **184**(1), 205–222 (2005).

Newman, B. G., Savage, S. B., and Schouella, D., "Model test on a wing section of a *Aeschna* dragonfly," in *Scale Effects in Animal Locomotion*, edited by Pedley, T. J. (Academic, London, 1977), pp. 445–477.

Okamoto, M., Yasuda, K., and Azuma, A., "Aerodynamic characteristics of the wings and body of a dragonfly," J. Exp. Biol. **199**, 281–294 (1996).

Peng, Z.-R., Huang, H., and Lu, X.-Y., "Collective locomotion of two self-propelled flapping plates with different propulsive capacities," Phys. Fluids **30**, 111901 (2018).

Perot, J. B., "An analysis of the fractional-step method," J. Comput. Phys. **108**(1), 51–58 (1993).

Rees, C., "Aerodynamic properties of an insect wing section and a smooth aerofoil compared," Nature **258**(13), 141–142 (1975).

Rudolph, R., "Aerodynamic properties of *Libellula Quadrimaculata L.* (Anisoptera. Libelludidea), and the flow," Odonatologica **7**, 49–58 (1977).

Ruppell, G., "Kinematic analysis of symmetrical flight maneuvers of odonata," J. Exp. Biol. **144**, 13–42 (1989).

Shahzad, A., Tian, F.-B., Young, J., and Lai, J. C., "Effects of hawkmoth-like flexibility on the aerodynamic performance of flapping wings with different shapes and aspect ratios," Phys. Fluids **30**, 091902-1–091902-19 (2018).

Vargas, A. and Mittal, R., "A computational study of the aerodynamic performance of a dragonfly wing," AIAA Paper 2004-2319, 2004.

Vargas, A., Mittal, R., and Dong, H., "A computational study of the aerodynamic performance of a dragon fly wing section in gliding flight," Bioinspiration Biomimetics **3**, 026004-1 (2008).

Wakeling, J. M. and Ellington, C. P., "Dragonfly flight: I. Gliding flight and steady-state aerodynamic forces," J. Exp. Biol. **200**, 543–556 (1997).

Xu, G. D., Duan, W. Y., and Xu, W. H., "The propulsion of two flapping foils with tandem configuration and vortex interactions," Phys. Fluids **29**, 097102 (2017).